

Karazin Kharkiv National University
Department of Physics and Technology



Technische Universität Darmstadt
Institut für Kernphysik



Transverse Electric Form Factors of
Low-Lying Transitions in
 ^{32}S , ^{48}Ca , ^{58}Ni , and ^{90}Zr
Measured with Electron Scattering at 180°

Diploma Thesis

Maksym Chernykh

Darmstadt 2004

Karazin Kharkiv National University
Department of Physics and Technology

Technische Universität Darmstadt
Institut für Kernphysik

Transverse Electric Form Factors of
Low-Lying Transitions in
 ^{32}S , ^{48}Ca , ^{58}Ni , and ^{90}Zr
Measured with Electron Scattering at 180°

Diploma Thesis

Maksym Chernykh

February 2004

Abstract

Inelastic electron scattering spectra for the nuclei ^{32}S , ^{48}Ca , ^{58}Ni , and ^{90}Zr measured at 180° have been analyzed to search for excitations of natural-parity states in the excitation region up to 7 MeV. Numerous cases were found by comparison with the available spectroscopic information and the cross sections were deduced. The experimental data for this work were obtained at the QCLAM spectrometer of the superconducting Darmstadt electron linear accelerator S - DALINAC using a system for the detection of scattered electrons at 180° . For all studied transitions cross sections and transverse form factors have been calculated.

A PWBA analysis including Coulomb distortion for ^{32}S has been carried out. The extracted transition strength for the second E2 transition to a 2^+ state $E_x = 4.282$ MeV in ^{32}S amounts to $B(E2) = (51 \pm 15) e^2\text{fm}^4$ and is in good agreement with photon scattering data. A shell model calculation using the unified *sd*-shell (USD) residual interaction suggests a purely transverse character of the measured cross sections for this transition. The momentum transfer dependence is reasonably described, but quantitatively overpredicted by a factor of 6.5.

In ^{58}Ni a preferable excitation of 2^+ states is observed. DWBA calculations with Quasiparticle-Phonon Model (QPM) wave functions predict the dominance of the transverse over the longitudinal cross sections. Experimental and theoretical cross sections agree qualitatively rather well, but quantitatively a theoretical overestimation by a factor 10 is observed.

In ^{90}Zr a preferable excitation of 3^- states is observed. A fragmentation region around 6 MeV is located for the $B(E3)$ strengths. Quasiparticle-Phonon Model calculations overpredict the cross sections by a factor 2 – 3.

Анотація

Спектри непружного розсіювання електронів для ядер ^{32}S , ^{48}Ca , ^{58}Ni та ^{90}Zr поміряні для кута 180° градусів були проаналізовані з метою пошуку рівнів збудження у енергетичному інтервалі до 7 MeV . Було знайдено чисельні випадки шляхом порівняння з доступною спектроскопічною інформацією та був визначений перетин розсіювання. Експериментальні дані для цієї роботи були отримані на спектрометрі QCLAM на суперпровідниковому лінійному прискорювачі електронів S-DALINAC у місті Дармштадт (Німеччина) з використанням системи для реєстрації розсіювання на 180° градусів. Для усіх розглянутих переходів були розраховані перетини розсіювання і поперечні форм-фактори.

Для ^{32}S був проведений PWBA аналіз, що включає кулонівське викривлення. Отримана інтенсивність переходу в стан 2^+ при $E = 4.282\text{ MeV}$ для ^{32}S , яке дорівнює $B(E2) = (51 \pm 15) e^2\text{fm}^4$, що добре узгоджується з даними для фотонного розсіювання. Розрахунки за оболонковою моделлю з використанням уніфікованої *sd*-оболонкової залишкової взаємодії припускають виключно поперечний характер виміряних перетинів розсіювання для цих переходів. Залежність від переданого імпульсу досить непогано описана, але з чисельним перевищенням на фактор 6.5.

Для ^{58}Ni спостерігається переважне збудження 2^+ рівнів. DWBA обчислення з використанням квазічастинково-фононої хвильової функції передбачає перевагу поперечного перетину розсіювання над повздовжним перетином. Експериментальні та

теоретичні перетини в залежності від переданого імпульсу розсіювання досить непогано узгоджуються, але з чисельним перевищенням на фактор 10.

Для ^{90}Zr спостерігається переважне збудження рівнів 3^- . Концентрація сили $V(E3)$ розташована навколо 6 MeV. Квазічастинково-фононні розрахунки перевищують експериментальні перетини розсіювання на фактор 2 – 3.

Contents

1	Introduction.....	9
2	Electron Scattering.....	12
2.1	Scattering Cross Section.....	12
2.2	Form Factors.....	13
2.3	Scattering at 180°.....	18
2.4	Higher-Order Corrections.....	20
2.4.1	Radiative Correction.....	20
2.4.2	Coulomb Correction.....	21
2.5	Shell Model.....	21
2.6	Quasiparticle-Phonon Model.....	23
3	Experimental Procedures.....	26
3.1	S-DALINAC and Experimental Facilities.....	26
3.2	180° Facility.....	28
3.2.1	QCLAM Spectrometer.....	29
3.3	Experimental Parameters.....	30
4	Analysis and Results.....	31
4.1	Fitting Procedure.....	32
4.2	Determination of Cross Sections and Form Factors.....	39
5	Model Comparison and Discussion.....	45
5.1	Calculations for ^{32}S	45
5.2	Comparison with Quasiparticle-Phonon Model Calculations.....	48
5.2.1	Calculations for ^{58}Ni	49

5.2.2	Calculations for ^{90}Zr	54
6	Summary and Outlook.....	58

1. Introduction

Nuclear structure studies using electromagnetic probes provide valuable information on the nuclear charge, current and magnetization densities [1, 2]. There are several reasons why electron scattering is a particularly powerful tool for studying nuclear structure [3]. Firstly, the basic interaction between the electron and the target nucleus is well known. It is the interaction of the charge and current density of the nucleus with the electromagnetic field of the passing electron. Secondly, the interaction is relatively weak, with a coupling constant of the order of $\alpha = 1/137$. It is the main advantage in comparison with strongly interacting particles, where the coupling constant is the order of unity and where the scattering mechanism cannot be clearly separated from structure effects in the target. In electron scattering the cross section can be immediately related to the transition matrix elements of the local charge, to the current density operators and to the structure of the target nucleus itself.

There is also an advantage of electron scattering over another widely used electromagnetic probe, real photon scattering. For a fixed energy loss ω of the electron, the three-momentum \mathbf{q} , transferred to the nucleus, can be varied as function of the four-momentum q_μ : $q_\mu^2 = \mathbf{q}^2 - \omega^2 > 0$. But with real photons for a given energy transfer there is only one possible momentum transfer since the mass of a real photon is zero: $q_\mu^2 = \mathbf{q}^2 - \omega^2 = 0$.

The investigation of the structure of the nucleus with inelastic electron scattering is one of the most important applications of the superconducting Darmstadt electron linear accelerator S-DALINAC at

the Institute of Nuclear Physics of the Darmstadt University of Technology [4, 5]. Due to its modern concept the S-DALINAC is a high-quality source of continuous electron beams with energies up to 130 MeV. For a momentum analysis of the scattered electrons in nuclear physics experiments the so-called QCLAM spectrometer [6] can be used. Due to its large solid angle and momentum acceptance this spectrometer is well suited for (e,e'x) coincidence [7] and 180° scattering experiments [8 - 10].

The longitudinal form factor usually dominates the cross sections for electric transitions, and there are only a few data on transverse form factors [11]. Electron scattering at 180° is unique for detecting the latter because of the strong suppression of longitudinal excitations including the radiative tail dominated by elastic scattering. Thus, electron scattering at 180° serves as a filter for transverse excitations and has been widely used for the investigation of magnetic excitations which are of purely transverse character [12].

Study of selected magnetic transitions [13 - 15] and M2 resonances [16, 17] is of particular interest at the S-DALINAC, where experimental data on ^{32}S , ^{48}Ca , ^{58}Ni , and ^{90}Zr have been taken. The purpose of the present work is an analysis of these data at low excitation energy, i.e. $E_x \leq 7$ MeV, searching for electric transitions. Such transitions are identified and analyzed in comparison to microscopic shell model (^{32}S) and Quasiparticle-Phonon Model (^{58}Ni , ^{90}Zr) calculations.

The work is divided into six chapters. The theoretical basis for an analysis of inelastic electron scattering cross sections and the above-mentioned models is presented in the second chapter. The third chapter provides a brief description of the experimental setup where

the present experiments were carried out. The data analysis is presented in the fourth chapter and a discussion with comparison to the model approaches in the fifth chapter. A short summary closes the thesis.

2. Electron Scattering

2.1 Scattering Cross Sections

The general electron scattering process is usually calculated assuming a single virtual photon exchange as shown in Fig. 2.1.

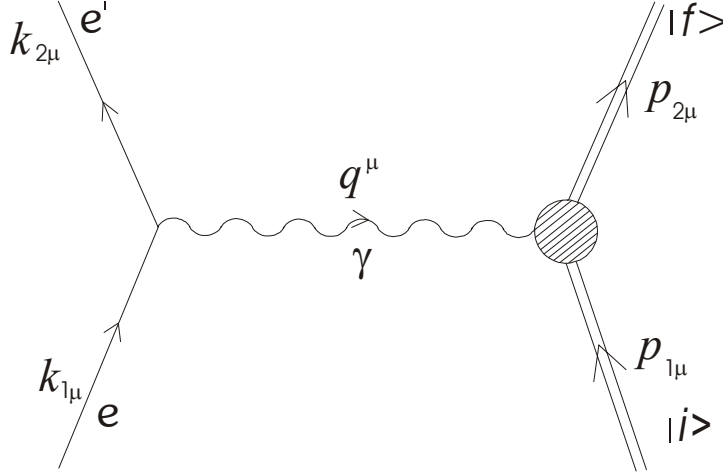


Fig. 2.1: Feynman diagram for lowest order (e,e') scattering process.

In this approximation, for any electromagnetic interaction with the nuclear system one needs only two independent structure functions to completely characterize the nuclear response to a single photon. Since higher-order terms, that is, the exchange of more than one virtual photon, involve higher powers of the fine-structure constant α , which characterizes the strength of the electromagnetic interaction, we expect this lowest-order diagram generally to account for most of the amplitude in electron scattering [18, 19]. Consider an electron initially with 4-momentum $k_{1\mu}$ scattering to $k_{2\mu}$ while the target with initial 4-momentum $P_{1\mu}$ goes from an initial state $|i\rangle$, to a final state $|f\rangle$, with a final momentum $P_{2\mu}$. The 3-momenta \mathbf{P} and \mathbf{k} and the associated energies E and ε are defined by $P_\mu = (\mathbf{P}, iE)$ and

$k_\mu = (\mathbf{k}, i\varepsilon)$. In the process a virtual photon with 4-momentum $q_\mu = k_{1\mu} - k_{2\mu} = P_{1\mu} - P_{2\mu}$ is exchanged. This involves an energy transfer ω and 3-momentum transfer \mathbf{q} , with $q^2 = \mathbf{q}^2 - \omega^2 \geq 0$. Thus electron scattering is restricted to the kinematic region where $\mathbf{q}^2 \geq \omega^2$.

Neglecting the electron mass (i.e., $m_e \ll \varepsilon_1$ or ε_2) and nuclear recoil, the cross section in the Plane Wave Born Approximation (PWBA) for this process can be written [20]

$$\begin{aligned} \frac{d\sigma}{d\Omega} = & \frac{8\pi\alpha^2 Z^2}{q_\mu^4} \frac{k_2}{k_1} \left[V_L(\theta) \frac{1}{2J_i + 1} \sum_{\lambda \geq 0} \left| \langle J_f \| \hat{M}_\lambda^{coul}(q) \| J_i \rangle \right|^2 \right. \\ & + V_T(\theta) \frac{1}{2J_i + 1} \left\{ \sum_{\lambda \geq 1} \left| \langle J_f \| \hat{T}_\lambda^{el}(q) \| J_i \rangle \right|^2 \right. \\ & \left. \left. + \sum_{\lambda \geq 1} \left| \langle J_f \| \hat{T}_\lambda^{mag}(q) \| J_i \rangle \right|^2 \right\} \right], \end{aligned} \quad (2.1)$$

where θ is the scattering angle, α the fine structure constant, Z the number of protons in the target nuclei and

$$V_L(\theta) = \frac{q_\mu^4}{q^4} 2k_1 k_2 \cos^2 \frac{\theta}{2} \quad (2.2)$$

$$V_T(\theta) = \frac{2k_1 k_2}{q^2} \sin^2 \frac{\theta}{2} \left[(k_1 + k_2)^2 - 2k_1 k_2 \cos^2 \frac{\theta}{2} \right]. \quad (2.3)$$

The operators $\hat{M}_\lambda^{coul}(q)$, $\hat{T}_\lambda^{el}(q)$, $\hat{T}_\lambda^{mag}(q)$, are the Coulomb, electric and magnetic operators of multipolarity λ , respectively. The quantities J_i and J_f are the initial and final total angular momenta of the target nucleus.

2.2 Form Factors

The cross section can also be expressed in terms of the nuclear form factor F as

$$\frac{d\sigma}{d\Omega} = 4\pi\sigma_{Mott} f_{rec} F^2(q, \theta). \quad (2.4)$$

The factor

$$\sigma_{Mott} = \frac{\alpha^2 (\hbar c)^2 \cos^2(\theta/2)}{4E_i^2 \sin^4(\theta/2)} \quad (2.5)$$

is the Mott cross section for scattering from a unit point charge while the recoil factor f_{rec} is given by

$$f_{rec} = \left[1 + \frac{2E_i \sin^2(\theta/2)}{M_T c^2} \right]^{-1}, \quad (2.6)$$

where M_T is the mass of the target nucleus.

In the Plane Wave Born Approximation the nuclear form factor can be decomposed into two terms as

$$F^2(\theta, q) = F_L^2(q) + \left[\frac{1}{2} + \tan^2\left(\frac{\theta}{2}\right) \right] \cdot F_T^2(q), \quad (2.7)$$

where the three-momentum transfer is related to the incident energy E_i , final energy E_f , and scattering angle θ by

$$q = \frac{\sqrt{2E_i(E_i - E_f)(1 - \cos\theta) + E_f^2}}{\hbar c}. \quad (2.8)$$

The longitudinal (F_L) and transverse (F_T) form factors are each dependent on q , but not on θ . This decomposition is due to the separation of the four-vector nuclear current density $\hat{J}^\mu(x) = (\hat{\mathbf{J}}(x), i\hat{\rho}(x))$ into components parallel and perpendicular to the momentum transfer \mathbf{q} . The component parallel to \mathbf{q} corresponds to an interaction of the electron with the nuclear charge density ρ , whereas the component perpendicular to \mathbf{q} involves the contribution of the nuclear convection current density $\hat{\mathbf{j}}_N(x)$ and magnetization density $\hat{\boldsymbol{\mu}}_N(x)$ since $\hat{\mathbf{J}}(x) = \hat{\mathbf{j}}_N(x) + \nabla \times \hat{\boldsymbol{\mu}}_N(x)$.

All the nuclear structure information is contained in the form factors

$$F_L^2(q) = \frac{1}{2J_i + 1} \sum_{\lambda \geq 0} \left| \langle J_f \| \hat{M}_\lambda^{coul}(q) \| J_i \rangle \right|^2, \quad (2.9)$$

$$F_T^2(q) = \frac{1}{2J_i + 1} \sum_{\lambda \geq 1} \left(\left| \langle J_f \| \hat{T}_\lambda^{el}(q) \| J_i \rangle \right|^2 + \left| \langle J_f \| \hat{T}_\lambda^{mag}(q) \| J_i \rangle \right|^2 \right). \quad (2.10)$$

The longitudinal and transverse form factors may be separated by fixing q and varying θ (Rosenbluth separation). Since the transverse current carries angular momentum ± 1 along \mathbf{q} while the Coulomb interaction carries angular momentum 0 along \mathbf{q} , they lead to different final nuclear states and do not interfere.

The Coulomb operators are defined using the vector spherical harmonics Y_λ^M and the spherical Bessel function $j_\lambda(qx)$ of order λ

$$\hat{M}_{\lambda M}^{coul}(q) \equiv \int dx j_\lambda(qx) Y_\lambda^M(\Omega_x) \hat{\rho}(x), \quad (2.11)$$

where $\lambda = 0, 1, 2$. We can also define transverse electric and magnetic multipole operators with natural parity, $\pi = (-1)^\lambda$ and unnatural parity, $\pi = (-1)^{\lambda+1}$, respectively,

$$\hat{T}_{\lambda M}^{el}(q) \equiv \frac{1}{q} \int dx \left\{ (\nabla \times \mathbf{j}_\lambda(q\mathbf{x}) Y_{\lambda\lambda}^M(\Omega_x)) \cdot \hat{\mathbf{J}}(\mathbf{x}) + q^2 \mathbf{j}_\lambda(q\mathbf{x}) Y_{\lambda\lambda}^M(\Omega_x) \cdot \hat{\boldsymbol{\mu}}_N(\mathbf{x}) \right\} \quad (2.12)$$

$$\hat{T}_{\lambda M}^{mag}(q) \equiv \int dx \left\{ \mathbf{j}_\lambda(q\mathbf{x}) Y_{\lambda\lambda}^M(\Omega_x) \cdot \hat{\mathbf{J}}(\mathbf{x}) + (\nabla \times \mathbf{j}_\lambda(q\mathbf{x}) Y_{\lambda\lambda}^M(\Omega_x)) \cdot \hat{\boldsymbol{\mu}}_N(\mathbf{x}) \right\}. \quad (2.13)$$

In the expansion, Eq. (2.10), only $\lambda \geq 1$ occurs, since the photon is massless and carries its spin ± 1 along, or opposite to, its direction of motion and thus we have $\lambda = 1, 2, 3, \dots$ with corresponding multipoles, carrying opposite parity. Hence the selection rules for the nuclear matrix elements follow from the angular momentum and parity properties of the multipole operators. From the properties of the Coulomb operator $\hat{M}_\lambda^{coul}(q)$ we have

$$\begin{aligned} \Delta\pi &= (-1)^\lambda, \\ |J_f - J_i| &\leq \lambda \leq J_f + J_i. \end{aligned} \quad (2.14)$$

Since the sum in Eq. (2.9) starts with $\lambda = 0$ we have the possibility of exciting a monopole transition $0^+ \rightarrow 0^+$ with electrons. The selection rules for electric and magnetic transitions are defined by the following expressions

$$\begin{aligned}\Delta\pi &= (-1)^\lambda && \text{transverse electric,} \\ \Delta\pi &= (-1)^{\lambda+1} && \text{transverse magnetic,} \\ |J_f - J_i| &\leq \lambda \leq J_f + J_i, \\ \lambda &\geq 1.\end{aligned}\tag{2.15}$$

The cross section can be written [21] in terms of the quantities $B(XL, q)$ ($X = C$ - Coulomb, E - electric or M - magnetic), which are the reduced transition probabilities for the inelastic transitions from the ground state of spin J_i to a final state of spin J_f (denoted by $B(XL, q) \uparrow$) and directly related to the matrix elements in Eqs. (2.9, 2.10)

$$\begin{aligned}\left(\frac{d\sigma}{d\Omega}\right)_{e\lambda} &= \alpha^2 a_\lambda q^{2\lambda} k_1^{-2} f_{rec} \left\{ \lambda(\lambda+1)^{-1} B(C\lambda, q, J_i \rightarrow J_f) V_L(\theta) \right. \\ &\quad \left. + B(E\lambda, q, J_i \rightarrow J_f) V_T(\theta) \right\},\end{aligned}\tag{2.16}$$

$$\left(\frac{d\sigma}{d\Omega}\right)_{m\lambda} = \alpha^2 a_\lambda q^{2\lambda} k_1^{-2} f_{rec} B(M\lambda, q, J_i \rightarrow J_f) V_T(\theta).\tag{2.17}$$

In these equations

$$a_\lambda = 4\pi\lambda^{-1}[(2\lambda+1)!!]^{-2},\tag{2.18}$$

$$q^2 = 2k_1^2(1 - \cos\theta)(1 - \omega/k_1) + \omega^2,\tag{2.19}$$

$$\omega = E_x/\hbar c, \quad k_1 = E_i/\hbar c,\tag{2.20}$$

where E_x and E_i are the excitation and the incident electron energies, respectively.

In photonuclear processes [22] the matrix elements for the excitation from the ground state of spin J_i to the excited state of spin J_f , $B(XL) \uparrow$, can be related to the de-excitation elements $B(XL) \downarrow$ by

$$B(XL) \downarrow = \frac{2J_i + 1}{2J_f + 1} B(XL) \uparrow. \quad (2.21)$$

The $B(XL)$ can be related to the transition width Γ by

$$\Gamma = 8\pi\alpha \sum_{L=1} \frac{L+1}{L[(2L+1)!]^2} \omega^{2L+1} [B(EL, \omega) \downarrow + B(ML, \omega) \downarrow]. \quad (2.22)$$

As an example for an M1 transition $0^+ \rightarrow 1^+$ this reduces to

$$\Gamma(eV) = 0.00387 [\omega(MeV)]^3 B(M1, \omega) \uparrow. \quad (2.23)$$

In order to obtain Γ from electron scattering one has to extrapolate the measured $B(XL, q)$ to $q = \omega$, the so-called photon point. In PWBA this extrapolation can be done in a fairly model-independent way. If $qr < 1$, then the spherical Bessel functions in the transition operators (Eq. 2.12) may be represented by a power series in qr , yielding for the reduced transition probabilities $B(CL, q)$ and $B(ML, q)$

$$\left[\frac{B(C\lambda, q)}{B(C\lambda, 0)} \right]^{\frac{1}{2}} = 1 - \frac{q^2}{2(2\lambda+3)} \frac{\langle r^{\lambda+2} \rangle_{tr}}{\langle r^\lambda \rangle_{tr}} + \frac{q^4}{8(2\lambda+3)(2\lambda+5)} \frac{\langle r^{\lambda+4} \rangle_{tr}}{\langle r^\lambda \rangle_{tr}} - \dots, \quad (2.24)$$

with $\lambda \geq 1$, and

$$\left[\frac{B(M\lambda, q)}{B(M\lambda, 0)} \right]^{\frac{1}{2}} = 1 - \frac{q^2}{2(2\lambda+3)} \frac{\lambda+3}{\lambda+1} \frac{\langle r^{\lambda+2} \rangle_{tr}}{\langle r^\lambda \rangle_{tr}} + \frac{q^4}{8(2\lambda+3)(2\lambda+5)} \frac{\lambda+5}{\lambda+1} \frac{\langle r^{\lambda+4} \rangle_{tr}}{\langle r^\lambda \rangle_{tr}} - \dots. \quad (2.25)$$

For the transverse electric part

$$\left\{ \frac{q^2 B(E\lambda, q)}{\lim_{q \rightarrow 0} [q^2 B(E\lambda, 0)]} \right\}^{\frac{1}{2}} = 1 - \frac{q^2}{2(2\lambda+3)} \frac{\lambda+3}{\lambda+1} \frac{\langle r^{\lambda+2} \rangle_{tr}}{\langle r^\lambda \rangle_{tr}}$$

$$+ \frac{q^4}{8(2\lambda+3)(2\lambda+5)} \frac{\lambda+5}{\lambda+1} \frac{\langle r^{\lambda+4} \rangle_{tr}}{\langle r^\lambda \rangle_{tr}} - \dots \quad (2.26)$$

If we consider the first terms in the expansion only we have at $q = \omega$ approximately

$$B(E\lambda, \omega) \cong B(C\lambda, \omega), \quad (2.27)$$

known as Siegert's Theorem [23].

Instead of the quantities $\langle r^{\lambda+1} \rangle_{tr}$ appearing in the above equations we can define a convenient "transition radius" R_{tr} which for $\lambda \geq 1$ is given by

$$R_{tr}^2 = \langle r^{\lambda+2} \rangle_{tr} / \langle r^\lambda \rangle_{tr}, \quad (2.28)$$

$$R_{tr}^4 = \langle r^{\lambda+4} \rangle_{tr} / \langle r^\lambda \rangle_{tr}, \quad (2.29)$$

$$R_{tr}^6 = \langle r^{\lambda+6} \rangle_{tr} / \langle r^\lambda \rangle_{tr}. \quad (2.30)$$

The equations can now be rewritten in terms of R_{tr} as

$$\left[\frac{q^2 B(E\lambda, q)}{\lim_{q \rightarrow 0} [q^2 B(E\lambda, 0)]} \right]^{\frac{1}{2}} = 1 - \frac{q^2}{2(2\lambda+3)} \frac{\lambda+3}{\lambda+1} R_{tr}^2 + \frac{q^4}{8(2\lambda+3)(2\lambda+5)} \frac{\lambda+5}{\lambda+1} R_{tr}^4 - \dots \quad (2.31)$$

$$\left[\frac{B(C\lambda, q)}{B(C\lambda, 0)} \right]^{\frac{1}{2}} = 1 - \frac{q^2}{2(2\lambda+3)} R_{tr}^2 + \frac{q^4}{8(2\lambda+3)(2\lambda+5)} R_{tr}^4 - \dots, \quad (2.32)$$

$$\left[\frac{B(M\lambda, q)}{B(M\lambda, 0)} \right]^{\frac{1}{2}} = 1 - \frac{q^2}{2(2\lambda+3)} \frac{\lambda+3}{\lambda+1} R_{tr}^2 + \frac{q^4}{8(2\lambda+3)(2\lambda+5)} \frac{\lambda+5}{\lambda+1} R_{tr}^4 - \dots \quad (2.33)$$

2.3 Scattering at 180°

A particularly attractive experimental tool for investigating magnetic and transverse electric excitations in nuclei with electron scattering is a detection system capable to measure at 180°. At 180°

the transverse contribution remains finite, whereas the longitudinal part of the inclusive (e,e') cross section vanishes nearly to zero, greatly suppressing the background and increasing the sensitivity for transverse transitions (Fig. 2.2). Thus, magnetic transitions, which are of purely transverse nature, are strongly enhanced at 180° where the elastic radiative tail is largely suppressed.

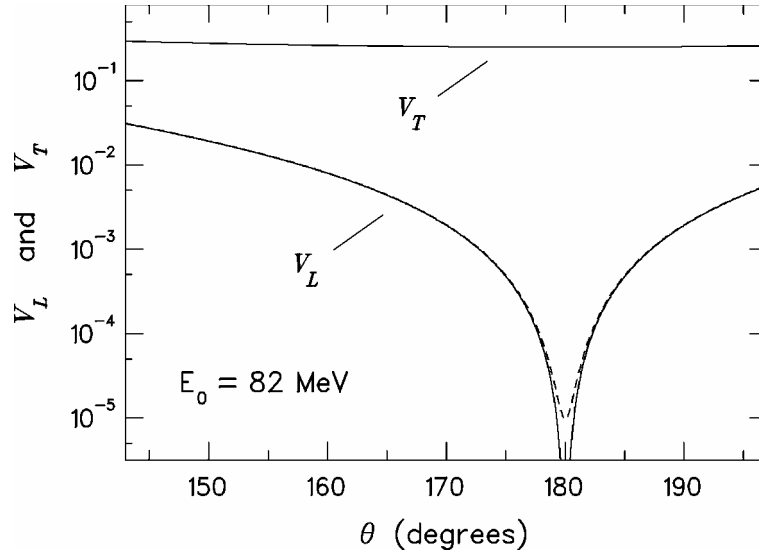


Fig. 2.2: Longitudinal V_L and transverse V_T kinematic factors for elastic scattering at an energy $E_0 = 82$ MeV. The dashed line represents the longitudinal kinematic factor, which is calculated taking into account the electron mass m_e .

Examining Eq. (2.2) we see that, at 180°

$$V_L(\pi) = \frac{q_\mu^4}{q^4} 2k_1 k_2 \cos^2 \frac{\pi}{2} = 0, \quad (2.34)$$

i.e. the longitudinal form factor vanishes leaving only the transverse form factor. This could also be inferred from the conservation of helicity. If we assume that, at relativistic velocities, the electron spin is aligned along or opposite its momentum, then for helicity to be conserved in 180° scattering, an electron spin flip must occur. Since

the longitudinal interaction cannot cause a spin flip, only the transverse electric and magnetic interactions are present. For transverse transitions of multipolarity λ , the cross section at 180° is

$$\left(\frac{d\sigma}{d\Omega}\right)_\lambda = \frac{1}{4} \alpha^2 a_\lambda q^{2\lambda} k_1^{-2} f_{rec} B(M\lambda/E, \lambda, q, J_i \rightarrow J_f), \quad (2.35)$$

with $V_T = 1/4$.

If we take into account the electron mass m_e , the exact behaviour of the longitudinal kinematic factor is described by the expression

$$V_L = \frac{(m_e c^2 / E_0)^2 \sin^2(\theta/2) + \cos^2(\theta/2)}{4 \sin^4(\theta/2)}. \quad (2.36)$$

2.4 Higher-Order Corrections

2.4.1 Radiative Correction

Since the electron has a very small mass, it scatters easily, generating radiation. When the electron scatters off a nucleus it interacts with the Coulomb radiation field emitting real and virtual photons and also loses energy due to atomic excitation and ionization. The experimental data show a broadening of a given peak, associated with soft photon production and a lower energy radiation tail resulting from hard photon emission. Every peak corresponding to a nuclear level has its own radiative tail and hence the tails of all the lower-lying peaks have to be subtracted from a given peak. After that the peak shape must be reconstructed for each level according to its own radiative tail.

The first of the radiative corrections, the Schwinger correction, accounts for the loss of the peak area due to those electrons degraded in energy due to emission of real soft photons as well as

emission and absorption of virtual photons of any energy. Bremsstrahlung corrections are for effects which cause an asymmetric distortion of the peak due to small angle scattering from electrons and nuclei other than the scattering nucleus. The third effect, Landau straggling, causes the broadening of the peak due to losses of energy from atomic excitation and ionization. The latter two corrections are proportional to the square of the target thickness t , while the Schwinger correction is linearly proportional to t .

2.4.2 Coulomb Correction

In the lowest order process considered we have used Plane Wave Born Approximation (PWBA), where the incoming and outgoing electrons are described by plane waves. The electron wave functions are distorted by the electromagnetic interaction with the nuclear charge distribution. Corrections for these distortions, called Coulomb distortions, may be calculated explicitly in the framework of Distorted Wave Born Approximation (DWBA). The measured cross section can be converted into equivalent plane wave values by multiplying with a factor,

$$f_c = [(d\sigma/d\Omega)_{DWBA}/(d\sigma/d\Omega)_{PWBA}], \quad (2.37)$$

and for low momentum transfers the f_c values are fairly insensitive [24] to variations in the excitation energy and R_{tr} , and almost independent of the nuclear model describing the excitation.

2.5 Shell Model

In the shell model approximation [25], a real nucleus is described by a nuclear Hamiltonian expressed in terms of neutron and proton coordinates and a two body interaction of the form

$$H = \sum_i T(r_i) + \sum_{i>j} V(r_i, r_j), \quad (2.38)$$

where i and j label the nucleons of the nucleus. Assuming that most of the effects $V(r_i, r_j)$ can be approximated by a central one-body potential $U(r_j)$, and the Hamiltonian can be rewritten as

$$H = H_1(r_1) + H_{12}(r_1, r_2), \quad (2.39)$$

where

$$H_1(r_i) = T(r_i) + U(r_i), \quad (2.40)$$

and

$$H_{12}(r_1, r_2) = T(r_1, r_2) - U(r_i). \quad (2.41)$$

The residual interaction H_{12} is assumed to be small so that it can be treated by perturbation theory.

A shell model calculation [26] involves a) the choice of the dominant central potential in H_1 , b) the calculation of the one-particle eigenstates of H_1 and the selection of the orbits of the model from this set, c) the construction of the multinucleon eigenstates of H_1 for a given number of nucleons and the chosen model orbits, d) the specification of the residual two-body interaction H_{12} and e) the evaluation of the matrix elements of H_{12} between the multinucleon eigenstates of the H_1 and the calculations of the eigenvalues and eigenvectors of this matrix.

Current shell model studies of sd -shell nuclei [27] are characterised by construction of the complete set of basis states that are available in the $d_{5/2} - s_{1/2} - d_{3/2}$ shells. After “defining the model basis space”, the effective single-particle potential for, and the effective two-body interaction between, the nucleons considered have to be determined. Results of calculations within the active model

space must ultimately be “renormalized” to account for the effects of excluded configurations in order to yield agreement with the experimental values.

2.6 Quasiparticle-Phonon Model

An alternative microscopic approach particularly useful for heavier nuclei is the Quasiparticle-Phonon Model (QPM) [28, 29]. It is based on a microscopic theory starting from the quasiparticle basis. In the Quasiparticle-Phonon Model excited states in even-even nuclei are considered as a combination of one-, two-, ..., n-phonon states built on the ground-state wave function $\Psi_{g.s.}$ which is treated as a phonon vacuum. Thus, the wave function of the state with momentum J and projection M has the form

$$\begin{aligned} \Psi_{\nu}(JM) = & \left\{ \sum_i R_i(J\nu) Q_{JM_i}^+ + \sum_{L_i L_i'} P_{L_i}^{L_i'}(J\nu) [Q_{L_i \mu_i}^+ Q_{L_i' \mu_i'}^+]_{JM} \right. \\ & \left. + \sum_{L_i L_i'} \sum_{J_i' L_i''} T_{L_i L_i'}^{J_i' L_i''}(J\nu) [[Q_{L_i \mu_i}^+ Q_{L_i' \mu_i'}^+]_{J_i M_i'} Q_{L_i'' \mu_i''}^+]_{JM} + \dots \right\} \Psi_{g.s.} \end{aligned} \quad (2.42)$$

with the definition

$$[Q_{L_i \mu_i}^+ Q_{L_i' \mu_i'}^+]_{JM} \equiv \sum_{\mu_i \mu_i'} \langle L_i \mu_i L_i' \mu_i' | JM \rangle Q_{L_i \mu_i}^+ Q_{L_i' \mu_i'}^+, \quad (2.43)$$

where $Q_{L_i \mu_i}^+$ is the phonon creation operator with angular momentum L_i , projection μ_i , and the Quasiparticle Random Phase Approximation (QRPA) root number i . Phonons are constructed as a linear combination of pairs of quasiparticle creation α_{jm}^+ and annihilation α_{jm} operators with the shell quantum numbers $jm \equiv |n, l, j, m\rangle$ as follows

$$Q_{L_i \mu_i}^+ = \frac{1}{2} \sum_{j j'}^{N, Z} \left\{ \psi_{j j'}^{L_i} [\alpha_{jm}^+ \alpha_{j'm'}^+]_{L_i \mu_i} + (-1)^{L_i - \mu_i} \phi_{j j'}^{L_i} [\alpha_{jm} \alpha_{j'm'}]_{L_i - \mu_i} \right\}. \quad (2.44)$$

To obtain the phonon basis (i.e., excitation energies ω_{Li} and structure coefficients $\psi_{jj'}^{Li}$ and $\phi_{jj'}^{Li}$), the QRPA equations for each J^π are solved with an effective Hamiltonian

$$H = H_{s.p.} + H_{pair} + H_{res} \quad (2.45)$$

where the first term describes the motion of independent nucleons in the self-consistent average field $U(r)$, the second term represents the pairing interaction, and the last term is the effective residual interaction between quasiparticles. The Hamiltonian H_{res} is considered in QPM to have a separable form, with the form factor of the residual interaction taken as $\partial U(r)/\partial r$. Among the phonon excitations there are both collective phonons such as the low-energy quadupole and octupole shape oscillations, and noncollective phonons, even practically pure two-quasiparticle modes.

With the obtained phonon basis, the Hamiltonian (2.45) can be rewritten in terms of phonon operators,

$$H = \sum_{L\mu i} \omega_{Li} Q_{L\mu i}^+ Q_{L\mu i} + \frac{1}{2\sqrt{2}} \sum_{L\mu i} \sum_{L'\mu' i'} \left\{ \bar{U}_{L'\mu'}^{L\mu i} (Li) [Q_{L'\mu' i'}^+ Q_{L\mu i}^+]_{L\mu} Q_{L\mu i} + H.c. \right\}. \quad (2.46)$$

The first term in Eq. (2.46) corresponds to the noninteracting phonon approximation. The second one describes the interaction between different parts of the wave function in Eq. (2.42) with the exchange of one phonon. Interaction matrix elements $\bar{U}_{L'\mu'}^{L\mu i} (Li)$ are calculated microscopically. The wave functions of the excited states in Eq. (2.42) are truncated to include terms up to three phonons. After diagonalization of the Hamiltonian in Eq. (2.45) on a set of excited states described by the wave function (2.42) one obtains the eigen energies of these states and their structure coefficients $R_i(J\nu)$, $P_{Li}^{L'i'}(J\nu)$, $T_{LiL'i'}^{JL'J'}(J\nu)$. Since the phonon operators are not ideal bosons,

the commutation relations must take into account their fermion structure in order not to violate the Pauli principle. In this approach, the Pauli principle is taken into account in the diagonal approximation, which is both sufficient for this kind of calculation and simplifies it. For additional details, see Refs. [30, 31].

3. Experimental Procedures

3.1 S-DALINAC and Experimental Facilities

The superconducting electron linear accelerator S-DALINAC [Fehler! Textmarke nicht definiert.] is in operation at the Institute of Nuclear Physics of the Darmstadt University of Technology since 1989. It is used for experiments on nuclear and radiation physics and since 1996 also as a driver for an infrared FEL [32, 33]. Using the high-frequency accelerating method and a dual beam recirculation, a continuous beam with energies between 2.5 and 130 MeV can be produced. A schematic layout of the S-DALINAC is shown in Fig. 3.1.

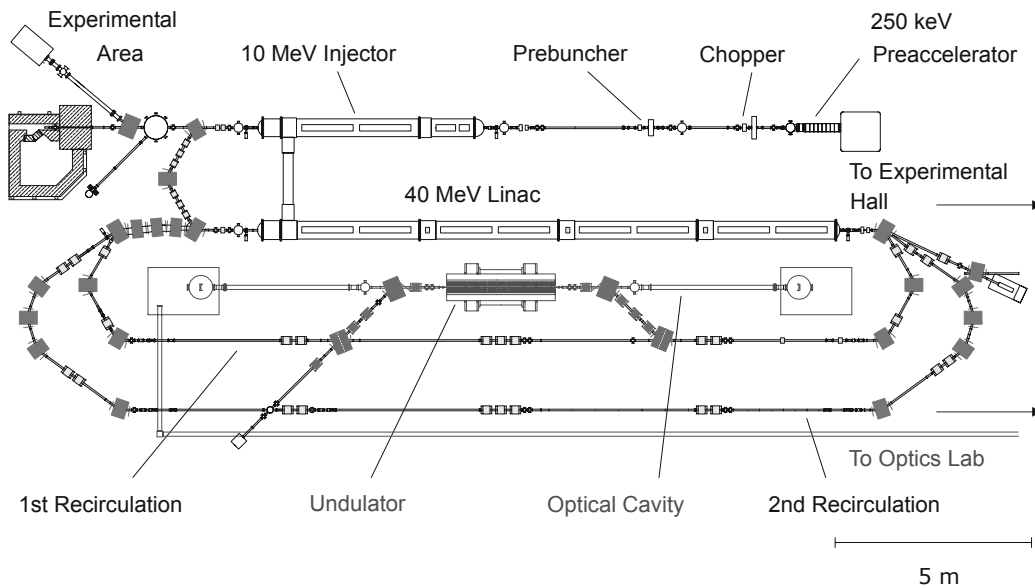


Fig. 3.1: Schematic layout of the S-DALINAC.

The electrons are emitted by a thermionic gun and then accelerated electrostatically to an energy of 250 keV. The required time structure of the electron beam for radio-frequency acceleration in a 3 GHz field is created by a chopper/prebuncher system operating at

room temperature. At the injector entrance the electron bunches arrive with a length of 5 ps separated by 333 ps with an average current up to 60 μA . The superconducting injector linac consists of one 2-cell, one 5-cell, and two standard 20-cell niobium cavities cooled to 2 K by liquid helium. The injector accelerates the beam up to an energy of 10 MeV. The beam can then enter an experimental area for low-energy experiments or can be injected by a 180° bending magnetic system into the superconducting main accelerator. It consists of eight 20-cell cavities and enables an energy increase up to 40 MeV.

After passing through the main linac the electron beam may be extracted to the experimental hall or it can be recirculated and reinjected once or twice. Additionally, in the first recirculation beam-line an infrared Free Electron Laser (FEL) is located. After at most three passes the electron beam with a maximum energy of up to 130 MeV is delivered to several experimental facilities, schematically shown in Fig. 3.2.

A wide range of electron scattering experiments is carried out using the QCLAM spectrometer (Pos. 5) and a high resolution energy-loss facility with a magic-angle spectrometer (Pos. 6). The QCLAM-spectrometer has a large angular and momentum acceptance and is used for $(e,e'x)$ coincidence and (e,e') at 180° experiments. The magic-angle spectrometer Lintott operates in the so-called “energy-loss” mode that enables to perform high resolution (e,e') experiments independently of the energy spread of the electron beam.

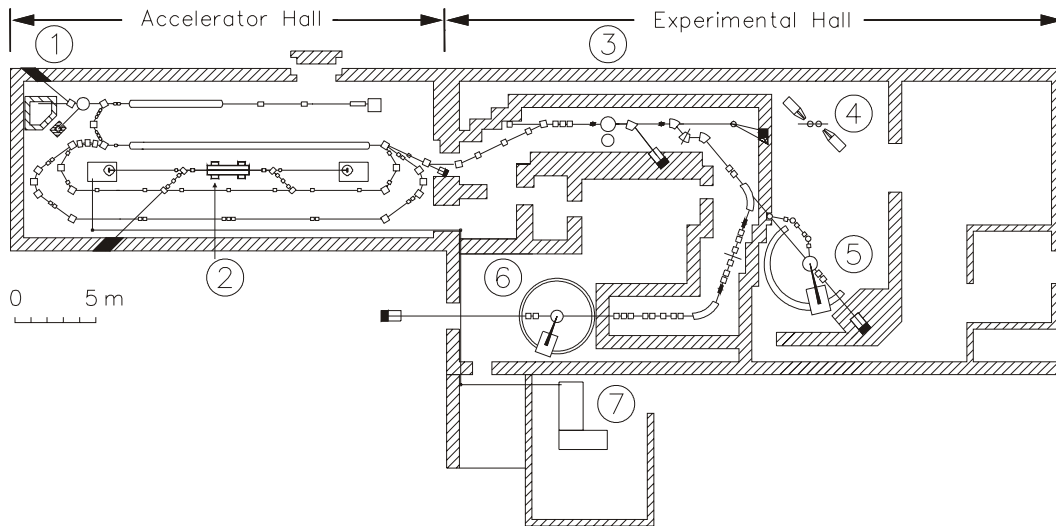


Fig. 3.2: Experimental facilities at the S-DALINAC.

Positions: 1 – photo activation and nuclear resonance fluorescence experiments, 2 - Free Electron Laser, 3 - high energy radiation physics, 4 - Compton scattering off nucleons, 5 - (e,e') at 180° and (e,e'x) experiments, 6 - (e,e')-experiments, 7 - optic experiments.

3.2 180° Facility

In addition to the apparatus necessary for performing electron scattering at forward angles, 180° scattering requires two additional items of beam transport equipment: a “separating magnet”, located between the target and the spectrometer, which deflects the incoming and 180°-scattered electrons in opposite directions, and a chicane of two or three magnets which deflects the incident beam before the separating magnet in such a way that the primary beam after the separating magnet is on the initial beam axis again. This system is illustrated in Fig. 3.3 and details are given in [34].

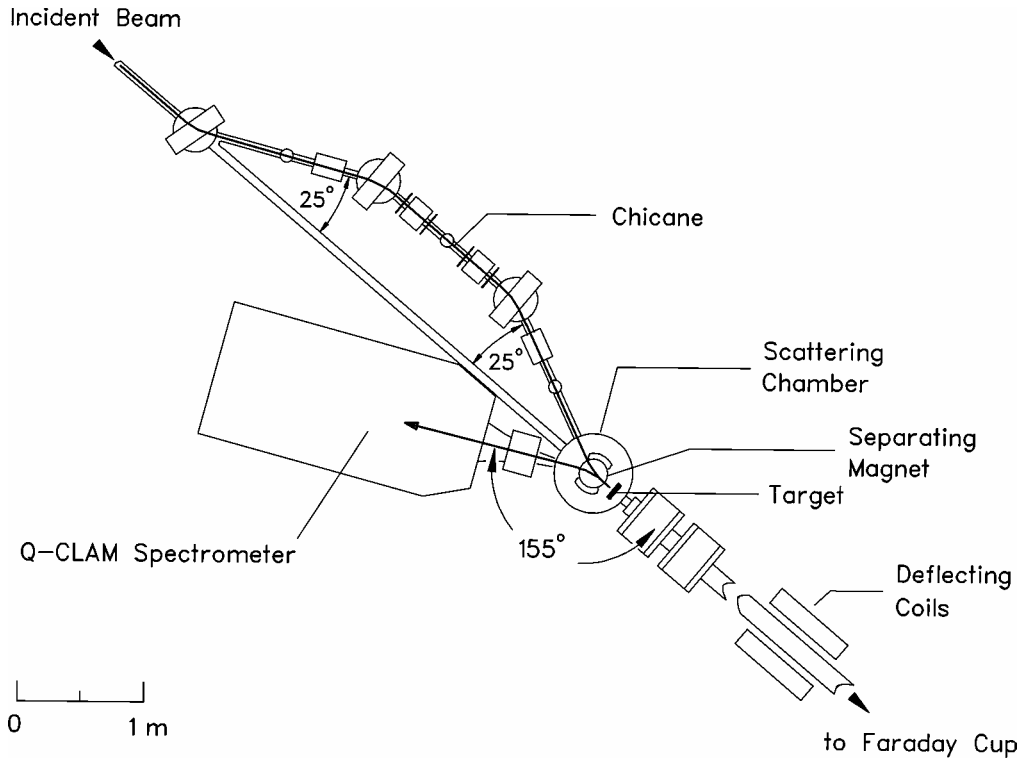


Fig. 3.3: Schematic view of the 180° system.

3.2.1 QCLAM Spectrometer

The QCLAM spectrometer is a large solid-angle, high-energy resolution magnetic spectrometer [35, 36]. It has a solid angle of up to 35 msr and a momentum acceptance of 20%. It contains two elements: a clamshell-type dipole magnet with a deflection angle of 120°, and a quadrupole magnet, which provides additional transverse focusing to increase the solid angle acceptance. The focal-plane instrumentation [37] consists of three multiwire drift chambers (two which measure the position in the dispersive direction, and one whose wires are rotated by 26.6° in orthogonal direction), a plastic scintillation counter serving as a trigger detector and a plexiglas Cherenkov detector for background suppression.

The chambers provide the horizontal and vertical positions and the vertical angle of the electron in the reference plane of the

detector system. The maximum central momentum of the spectrometer is 200 MeV/c. Because the 180° components were initially designed for a lower-energy accelerator at the University of Illinois, the 180° system is presently limited to a maximum electron energy of about 95 MeV.

3.3 Experimental Parameters

In the experiments four targets were irradiated Li_2S (28 mg/cm²), ^{48}Ca (10.2 mg/cm²), ^{58}Ni (7.6 mg/cm²), and ^{90}Zr (19.8 mg/cm²). The target Li_2S represented a foil with natural isotope content, i.e. 61.72% ^7Li , 4.95% ^6Li , 31.67% ^{32}S , 0.25% ^{33}S , 1.4% ^{34}S , and 0.005% ^{36}S . The effective thickness for ^{32}S was 17.86 mg/cm². For the ^{48}Ca , ^{58}Ni , and ^{90}Zr targets the isotopic enrichment was more than 97%. For each element two or three spectra at the incident energies E_0 from 42.2 up to 82.3 MeV were measured. This corresponds to momentum transfers q from 0.37 fm⁻¹ up to 0.83 fm⁻¹. The energy resolution ΔE was between 50 and 100 keV. All spectra were measured up to approximately 14 MeV. The experimental parameters are summarized in Table 1. In this work the low energy region in the spectra up to 7 MeV of excitation energy has been analyzed.

A detailed description of the data extraction procedure is given in [38]. For background suppression the so-called time of flight method [39] was used. The channel counting rates of the spectra for ^{32}S , ^{48}Ca and ^{90}Zr were normalized to the angular acceptance of the spectrometer and to the charge accumulated in the Faraday cup. Also dead time correction was applied. The spectra for ^{58}Ni were normalized by comparison to the measurements on ^{12}C [40].

Table 1: The main parameters of the (e,e') experiments at the S-DALINAC.

Element	Thickness (mg/cm ²)	E ₀ (MeV)	E _x (MeV)	q(fm ⁻¹)	ΔE(keV)
³² S	17.86	82.2	0.0 – 14.4	0.77 – 0.83	100
		66.4	3.2 – 14.6	0.62 – 0.65	68
		42.2	3.7 – 11.3	0.38 – 0.41	75
⁴⁸ Ca	10.2	82.1	3.0 – 16.0	0.76 – 0.81	66
		66.4	3.0 – 15.2	0.60 – 0.66	57
		42.4	3.5 – 11.4	0.37 – 0.41	50
⁵⁸ Ni	7.6	65.4	0.0 – 11.1	0.60 – 0.66	80
		56.6	0.0 – 9.5	0.52 – 0.57	76
⁹⁰ Zr	19.8	82.3	3.0 – 16.0	0.77 – 0.82	72
		66.4	3.0 – 15.2	0.60 – 0.66	61
		42.7	3.5 – 11.0	0.37 – 0.41	55

In this work the following contributions determined the systematic error

- uncertainty with respect to the determination of the accumulated charge in the Faraday cup ($\approx 5\%$),
- inaccuracy of the solid angle ($\approx 7\%$),
- target inhomogeneities ($\approx 5\%$),
- error in the dead time correction ($< 2\%$).

Thus, the squared averaged total contribution of the instrumental error amounts approximately to 10%. In the following tables only statistical errors are indicated.

4. Analysis and Results

4.1 Fitting Procedure

An example of the fitting procedure is presented in Fig. 4.1 for ^{58}Ni . The spectra correspond to the incident electron energies of 65.4 MeV and 56.6 MeV.

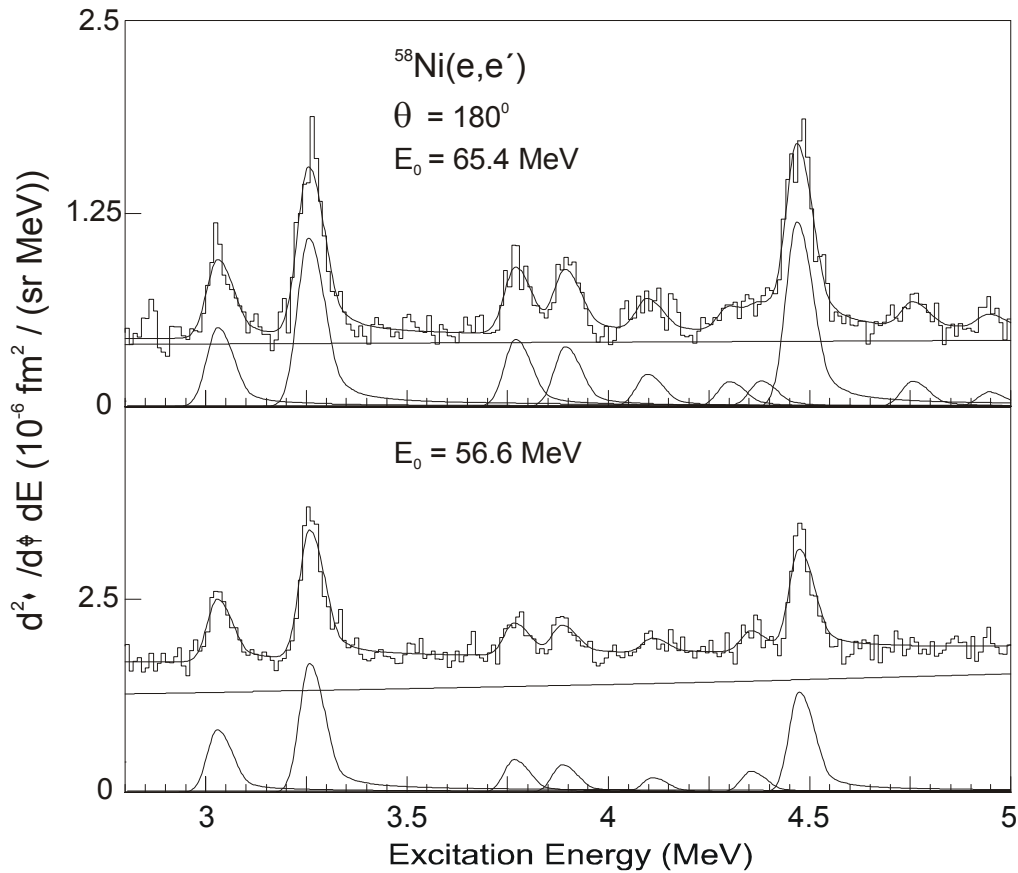


Fig. 4.1: Electron scattering spectra of the reaction $^{58}\text{Ni}(e,e')$ taken at $E_0 = 65.4$ MeV and $E_0 = 56.6$ MeV within the excitation energy range $E_x = 2.8 - 5.0$ MeV. The decomposition into peaks and background is shown.

The spectra were analysed using the program FIT [41, 42], that has been routinely used to analyse data from electron scattering

and several other reactions. In this program the fitting function consists of a background function plus a sum over individual peaks y_i that may be represented in terms of the excitation energy x as

$$F(x) = B(x) + \sum_{peaks} y_i(x), \quad (4.1)$$

where $B(x)$ is the background function given by a polynomial of second degree

$$B(x) = b_0 + b_1x + b_2x^2. \quad (4.2)$$

The background consists of the radiative tails of each line and the instrumental background. This and all observable transitions were fitted simultaneously.

The shape of a peak was described by a special function integrated in the FIT program, which takes into account the radiative tail as well as the Gaussian distribution of the peak. This function consists of three parts: a Gaussian rising flank of width σ_1 , a Gaussian dropping flank of width σ_2 and a hyperbolic function simulating the radiative tail. These three functions are connected to each other and form a smoothly differentiable function, which is represented by the following expression:

$$y = y_0 \cdot \begin{cases} \exp[-C(x-x_0)^2/\sigma_1^2] & x < x_0 \\ \exp[-C(x-x_0)^2/\sigma_2^2] & x_0 < x \leq x_0 + \eta\sigma_2, \\ A/(B+x-x_0)^\gamma & x > x_0 + \eta\sigma_2 \end{cases} \quad (4.3)$$

where x_0 is the energy of the peak maximum, y_0 is the counting rate in the peak maximum, σ_1^2 and σ_2^2 are the variances of the Gauss functions for $E_x < x_0$ and $E_x > x_0$, η is the starting point of the radiative tail in units of σ_2 and γ is the exponent of the hyperbolic function. The factors A, B and C result from the condition of the smoothly differentiable connection of the individual functions at the

interconnection points x_0 and $x_0 + \eta\sigma_2$. The adaptation of the model functions for the spectral lines took place in a given energy interval simultaneously with the adaptation of the background polynomial.

The line shape was determined from the most prominent transitions in each spectrum and the same parameters were used for all transitions in a spectrum. In addition, relative positions of the lines could be fixed. This is particularly useful at higher excitation energies, where the level density becomes high.

The results for all analyzed spectra measured for the nuclei ^{32}S , ^{48}Ni , ^{58}Ca , and ^{90}Zr are presented in Figs. 4.2 - 4.5.

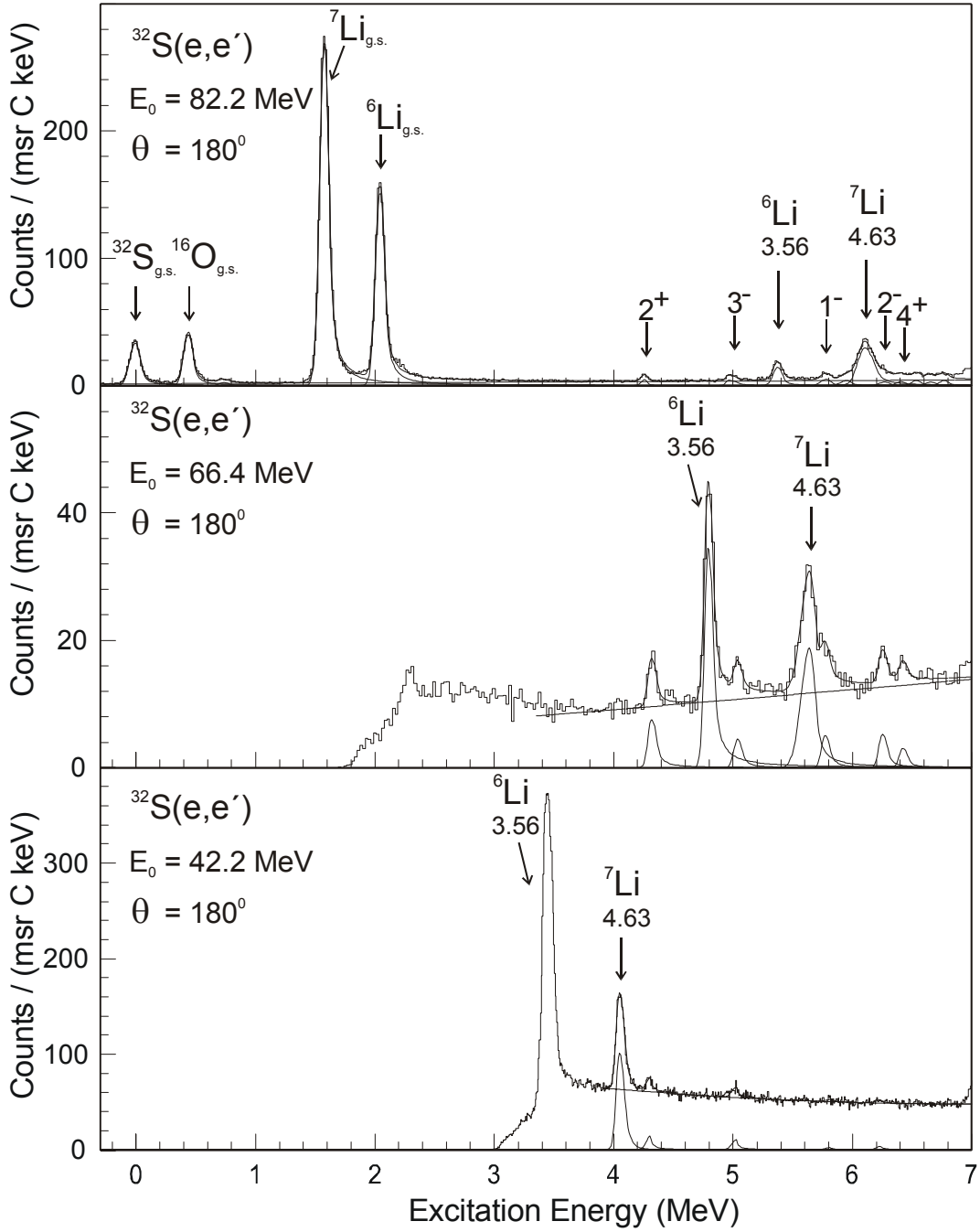


Fig. 4.2: Analysis of the electron scattering spectra for the reaction $^{32}\text{S}(e,e')$ for the beam energies $E_0 = 82.2$ MeV, $E_0 = 66.4$ MeV and $E_0 = 42.2$ MeV in the excitation energy range $E_x = 0 - 7$ MeV.

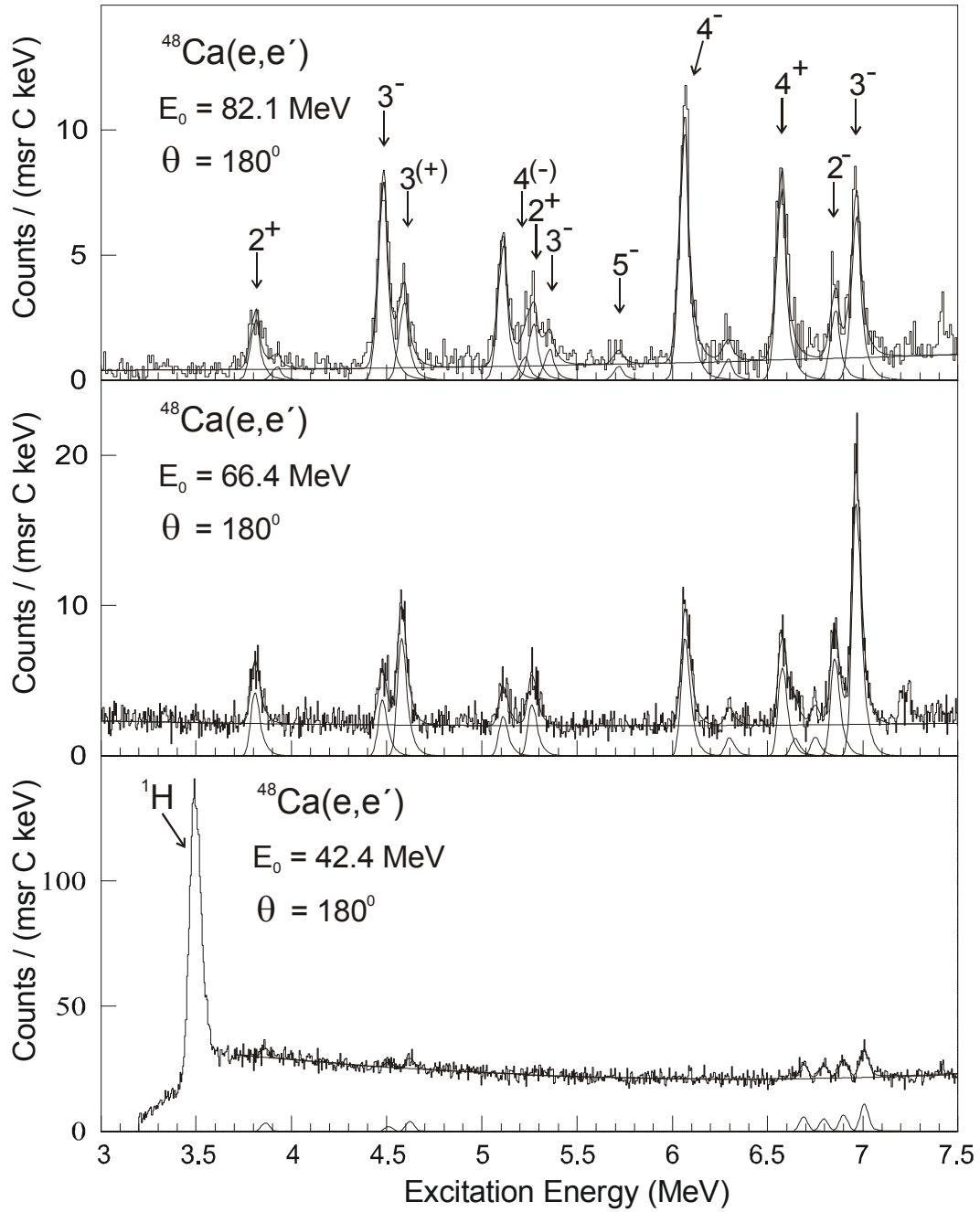


Fig. 4.3: Analysis of the electron scattering spectra for the reaction $^{48}\text{Ca}(e,e')$ for the beam energies $E_0 = 82.1$ MeV, $E_0 = 66.4$ MeV and $E_0 = 42.4$ MeV in the excitation energy range $E_x = 3 - 7.5$ MeV.

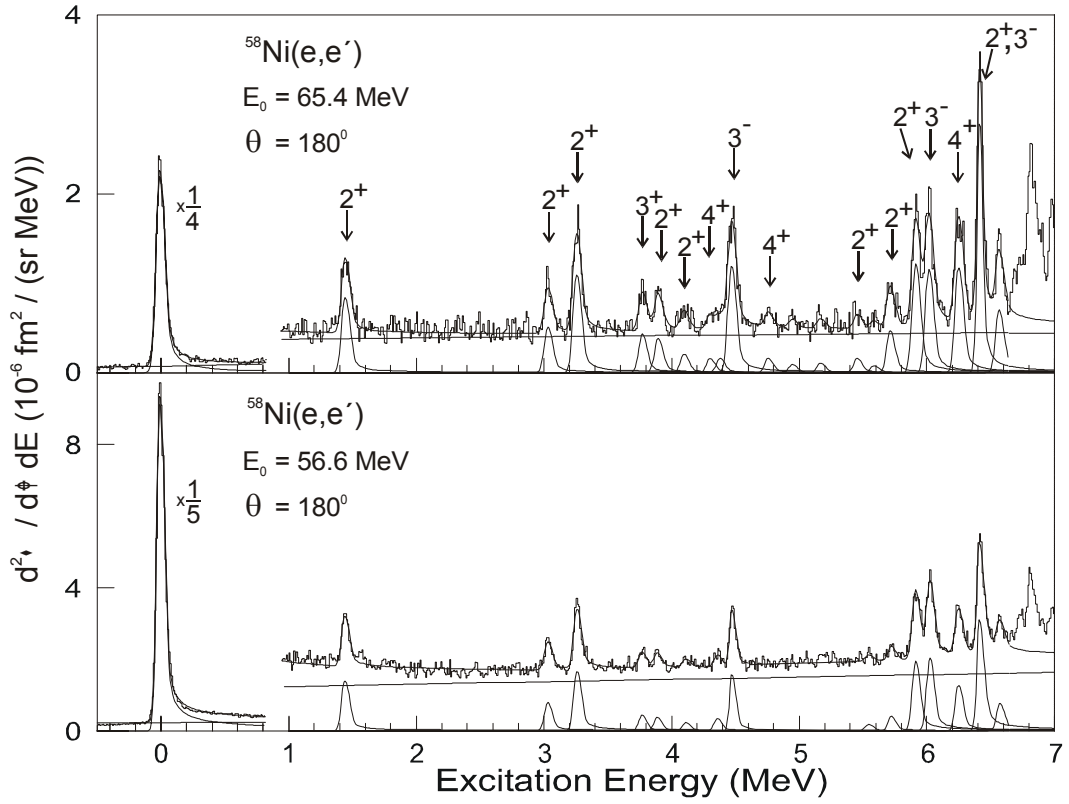


Fig. 4.4: Analysis of the electron scattering spectra for the reaction $^{58}\text{Ni}(e, e')$ for the beam energies $E_0 = 65.4 \text{ MeV}$ and $E_0 = 56.6 \text{ MeV}$ in the excitation energy range $E_x = 0 - 7 \text{ MeV}$.

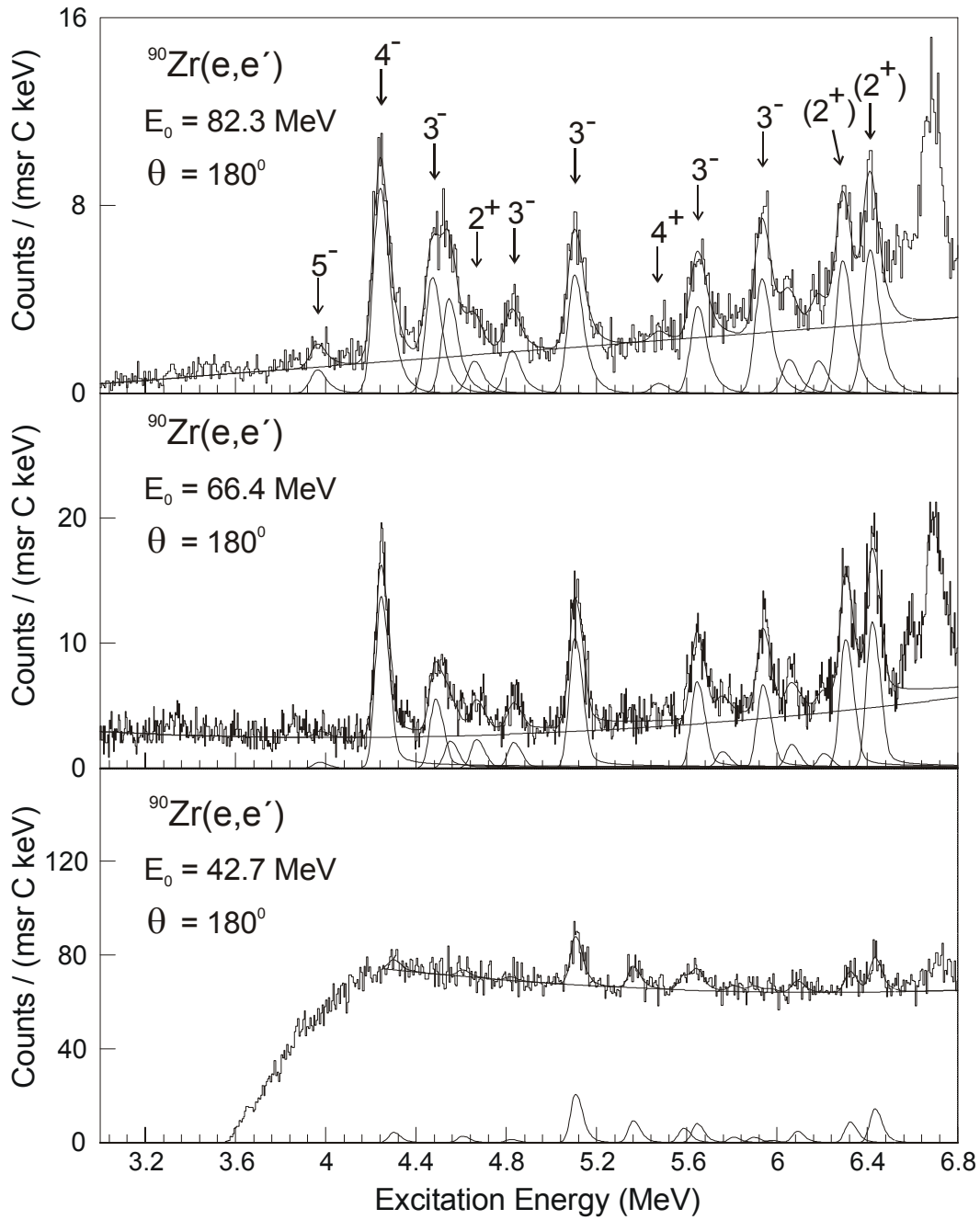


Fig. 4.5: Analysis of the electron scattering spectra for the reaction $^{90}\text{Zr}(e,e')$ for the beam energies $E_0 = 82.3 \text{ MeV}$, $E_0 = 66.4 \text{ MeV}$ and $E_0 = 42.7 \text{ MeV}$ in the excitation energy range $E_x = 3 - 6.8 \text{ MeV}$.

4.2 Determination of Cross Sections and Form Factors

In order to determine the peak area, the fit function under each peak was integrated. The contributions of the radiative tails to the full peak area were calculated with standard formulas for (e,e') radiative correction functions [43]. Since the radiative tail stretches in principle to infinity, it is necessary to fix an upper integration limit. In the FIT program the lower integration limit corresponds to the beginning of the Gaussian rising flank and the upper integration limit corresponds to 5 widths of the Gaussian dropping flank σ_2 , i.e. $E_{upper} = E_0 + 5\sigma_2$. This parameter was chosen to minimize the uncertainty in the determination of the area under the peak. Then the differential cross section is determined by the following expression:

$$\frac{d\sigma}{d\Omega} = N \cdot \frac{M}{\rho N_A} \cdot 1.72 \cdot 10^{10} \text{ fm}^2 / \text{sr} \quad (4.4)$$

where M [MeV/c²] – the mass of the target nuclei, N_A [mol⁻¹] – the Avogadro constant, ρ [g/cm²] – the target thickness and N [1/C msr] - the peak area normalized to the spectrometer solid angle and the current accumulated in the Faraday cup during the measurement.

Under 180° elastic scattering is strongly suppressed for targets with ground state $J^\pi = 0^+$ [Eq. (2.2)]. Since in 180° experiments the effective scattering angle θ_{eff} is not exactly equal to 180°, an elastic line is still visible in the spectra and the relative calculation of the inelastic scattering cross section is possible in principle. In this work the average effective scattering angle θ_{eff} was 178°. However, a variation of 0.1° from $\theta_{eff} = 178^\circ$ changes the elastic cross section by more than 10%. A precise determination of the elastic cross section and the relative calculation of the inelastic cross section are thus not

possible because the effective angle can be determined only with an uncertainty of approximately 0.1° .

The Tables 2 – 5 summarize the kinematics, the experimental cross sections, and the deduced form factors (assuming they are purely transverse) for all transitions below $E_x = 7$ MeV of the targets investigated. In these tables E_x is the observed excitation energy, J^π the spin-parity of the excited state, E_0 is the incident electron energy, q_{eff} the effective momentum transfer, $d\sigma/d\Omega$ and $|F_t|^2$ are the experimental cross section and the squared transverse form factor, and ‘Error’ is the statistical uncertainty in the peak area determination. The effective momentum transfer q_{eff} is defined by the relation

$$q_{eff} = q \left(1 + \frac{3\sqrt{3}Ze^2}{2\sqrt{5}E_0R_c} \right), \quad (4.5)$$

where R_c is the root-mean-square radius [44], and E_0 is the energy of the incident electrons.

The spin-parity identification of observed states is based on a comparison with spectroscopic data from the Nuclear Data Sheets [45]. In principle, the form factors exhibit a characteristic momentum transfer dependence with a maximum at a specific q value (respectively a small region of q values) for the transferred angular momentum. Due to the small number of experimental points an accurate spin-parity assignment of the transitions based on the (e,e') data cannot be done. Nevertheless, the comparison to the NDS shows the preferable population of 2^+ states in ^{58}Ni and 3^- states in ^{90}Zr .

Table 2: Cross sections and transverse form factors of the inelastic electron scattering on ^{32}S under 180° . The excitation energy E_x is determined as an average of the excitation energies in all measured spectra. Errors indicate the statistical uncertainty of the peak area determination.

E_x (MeV)	J^π	E_0 (MeV)	q (fm^{-1})	q_{eff} (fm^{-1})	$d\sigma/d\Omega$ (fm^2/sr)	$ F_t ^2$	Error (%)
0	0^+	82.2	0.833	0.915	3.293E-07	0	3.0
4.281(9)	2^+	42.2	0.406	0.483	8.935E-08	1.201E-06	22.7
		66.4	0.651	0.730	6.473E-08	2.158E-06	10.9
		82.2	0.811	0.891	2.805E-08	1.435E-06	15.4
5.017(10)	3^-	42.2	0.402	0.479	6.743E-08	9.065E-07	21.6
		66.4	0.647	0.726	3.823E-08	1.274E-06	20.1
		82.2	0.808	0.887	4.103E-08	2.099E-06	20.8
5.798(10)	1^-	42.2	0.398	0.474	1.435E-08	1.929E-07	57.4
		66.4	0.644	0.722	4.308E-08	1.436E-06	22.2
		82.2	0.803	0.882	4.974E-08	2.544E-06	10.3
6.264(11)	2^-	42.2	0.396	0.472	2.202E-08	2.960E-07	40.3
		66.4	0.641	0.719	4.460E-08	1.487E-06	15.8
		82.2	0.801	0.879	2.802E-08	1.433E-06	45.7
6.432(8)	4^+	66.4	0.640	0.718	2.563E-08	8.543E-07	24.9
		82.2	0.800	0.879	2.931E-08	1.499E-06	20.2
6.569(9)		82.2	0.800	0.878	3.658E-08	1.871E-06	15.2
6.690(13)		82.2	0.799	0.877	2.556E-08	1.307E-06	21.0
6.803(9)	4^+	82.2	0.798	0.877	3.614E-08	1.848E-06	14.7

Table 3: Cross sections and transverse form factors of the inelastic electron scattering on ^{48}Ca under 180° . The excitation energy E_x is determined as an average of the excitation energies in all measured spectra. Errors indicate the statistical uncertainty of the peak area determination.

E_x (MeV)	J^π	E_0 (MeV)	q (fm^{-1})	q_{eff} (fm^{-1})	$d\sigma/d\Omega$ (fm^2/sr)	$ F_t ^2$	Error (%)
3.844(3)	2^+	42.4	0.410	0.499	3.072E-08	2.667E-07	26.1
		66.4	0.653	0.743	4.492E-08	9.570E-07	7.5
		82.1	0.812	0.903	2.818E-08	9.185E-07	12.4
4.507(5)	3^-	42.4	0.407	0.495	1.639E-08	1.423E-07	42.0
		66.4	0.650	0.740	3.979E-08	8.478E-07	8.2
		82.1	0.809	0.899	9.167E-08	2.988E-06	6.8
4.615(3)	3	42.4	0.406	0.494	3.692E-08	3.206E-07	19.0
		66.4	0.649	0.739	8.303E-08	1.769E-06	5.3
		82.1	0.808	0.899	3.598E-08	1.173E-06	12.2
5.14(3)		66.4	0.647	0.736	2.779E-08	5.921E-07	9.9
		82.1	0.806	0.896	6.241E-08	2.034E-06	8.0
5.249(20)		82.1	0.805	0.895	1.079E-08	3.518E-07	70.8
5.297(5)	2^+	66.4	0.646	0.735	3.620E-08	7.713E-07	8.3
		82.1	0.805	0.895	2.589E-08	8.440E-07	30.5
5.379(8)	3^-	82.1	0.805	0.894	1.439E-08	4.690E-07	22.6
5.744(13)	5^-	82.1	0.803	0.892	6.522E-09	2.126E-07	38.4
6.097(2)	4^-	66.4	0.642	0.730	8.317E-08	1.772E-06	4.8
		82.1	0.801	0.890	1.143E-07	3.726E-06	5.6
6.328(6)	2^+	66.4	0.641	0.729	1.279E-08	2.724E-07	19.6
		82.1	0.800	0.889	9.791E-09	3.191E-07	29.4
6.688(5)		42.4	0.396	0.481	5.144E-08	4.466E-07	13.4
6.608(2)	4^+	66.4	0.639	0.727	6.214E-08	1.324E-06	6.6
		82.1	0.798	0.887	8.860E-08	2.888E-06	6.5
6.794(5)	2^+	42.4	0.395	0.481	4.471E-08	3.882E-07	14.8
6.881(2)	2^-	42.4	0.395	0.480	5.918E-08	5.138E-07	11.6
		66.4	0.638	0.726	6.852E-08	1.460E-06	5.7
		82.1	0.797	0.886	3.220E-08	1.049E-06	13.0
7.002(2)	3^-	42.4	0.394	0.479	9.865E-08	8.566E-07	9.1
		66.4	0.637	0.725	1.787E-07	3.808E-06	3.2
		82.1	0.796	0.885	7.595E-08	2.475E-06	7.3

Table 4: Cross sections and transverse form factors of the inelastic electron scattering on ^{58}Ni under 180° . The excitation energy E_x is determined as an average of the excitation energies in all measured spectra. Errors indicate the statistical uncertainty of the peak area determination.

E_x (MeV)	J^π	E_0 (MeV)	q (fm^{-1})	q_{eff} (fm^{-1})	$d\sigma/d\Omega$ (fm^2/sr)	$ F_t ^2$	Error (%)
0	0^+	56.6	0.573	0.697	4.973E-06	0	0.6
		65.4	0.663	0.787	1.044E-06	0	1.4
1.444(2)	2^+	56.6	0.566	0.689	1.525E-07	1.202E-06	5.6
		65.4	0.655	0.778	9.762E-08	1.030E-06	6.0
3.036(3)	2^+	56.6	0.558	0.679	8.751E-08	6.909E-07	9.0
		65.4	0.647	0.768	5.934E-08	6.263E-07	8.9
3.264(1)	2^+	56.6	0.557	0.677	1.800E-07	1.425E-06	4.9
		65.4	0.646	0.767	1.268E-07	1.339E-06	5.1
3.776(4)	3^+	56.6	0.554	0.674	4.571E-08	3.607E-07	15.8
		65.4	0.643	0.764	5.047E-08	5.320E-07	10.3
3.898(5)	2^+	56.6	0.554	0.673	3.853E-08	3.046E-07	18.4
		65.4	0.643	0.763	4.496E-08	4.742E-07	11.6
4.113(9)	2^+	56.6	0.553	0.672	2.027E-08	1.603E-07	29.6
		65.4	0.642	0.762	2.408E-08	2.537E-07	19.1
4.310(15)	4^+	65.4	0.641	0.761	1.876E-08	1.980E-07	31.0
4.378(11)		56.6	0.551	0.670	2.908E-08	2.292E-07	21.1
		65.4	0.640	0.760	1.921E-08	2.025E-07	30.7
4.478(2)	3^-	56.6	0.551	0.670	1.404E-07	1.106E-06	8.1
		65.4	0.640	0.760	1.387E-07	1.465E-06	5.4
4.767(11)	4^+	65.4	0.638	0.758	1.896E-08	2.000E-07	24.8
4.957(18)		65.4	0.638	0.757	1.073E-08	1.131E-07	41.9
5.178(16)		65.4	0.636	0.755	1.234E-08	1.302E-07	36.6
5.466(11)		65.4	0.635	0.754	1.905E-08	2.001E-07	24.2
5.575(14)	2^+	56.6	0.545	0.663	1.805E-08	1.427E-07	39.0
		65.4	0.634	0.753	9.151E-09	9.650E-08	49.2
5.730(4)	2^+	56.6	0.544	0.662	3.993E-08	3.153E-07	18.0
		65.4	0.634	0.752	5.464E-08	5.759E-07	9.9
5.924(1)	2^+	56.6	0.543	0.661	2.031E-07	1.603E-06	4.7
		65.4	0.633	0.751	1.412E-07	1.488E-06	5.2
6.032(2)	3^-	56.6	0.543	0.660	2.110E-07	1.670E-06	4.5
		65.4	0.632	0.750	1.340E-07	1.413E-06	5.6
6.261(2)	4^+	56.6	0.542	0.659	1.236E-07	9.779E-07	7.1
		65.4	0.631	0.749	1.363E-07	1.437E-06	5.1
6.424(2)	$2^+(3^-)$	56.6	0.541	0.658	2.902E-07	2.292E-06	5.1
		65.4	0.630	0.748	2.345E-07	2.475E-06	3.8
6.583(3)	$2^+(4^+)$	56.6	0.540	0.657	6.778E-08	5.351E-07	11.9
		65.4	0.629	0.747	8.194E-08	8.639E-07	8.3

Table 5: Cross sections and transverse form factors of the inelastic electron scattering on ^{90}Zr under 180° . The excitation energy E_x is determined as an average of the excitation energies in all measured spectra. Errors indicate the statistical uncertainty of the peak area determination.

E_x (MeV)	J^π	E_0 (MeV)	q (fm^{-1})	q_{eff} (fm^{-1})	$d\sigma/d\Omega$ (fm^2/sr)	$ F_t ^2$	Error (%)
3.969(8)	5^-	82.3	0.814	0.968	1.526E-08	1.248E-07	16.8
4.250(2)	4^-	66.35	0.651	0.803	1.769E-07	9.393E-07	4.2
		82.3	0.812	0.966	1.349E-07	1.103E-06	4.1
4.309(13)		42.72	0.411	0.561	4.778E-07	1.051E-07	40.9
4.487(3)	3^-	66.35	0.650	0.802	7.104E-08	3.773E-07	10.0
		82.3	0.811	0.964	7.616E-08	6.225E-07	9.3
4.556(7)		42.72	0.409	0.559	3.145E-08	6.919E-08	54.4
		66.35	0.649	0.801	2.792E-08	1.483E-07	23.2
		82.3	0.811	0.964	6.186E-08	5.057E-07	10.7
4.671(5)	2^+	66.35	0.649	0.801	2.958E-08	1.571E-07	14.9
		82.3	0.810	0.963	2.055E-08	1.680E-07	19.0
4.833(12)	3^-	42.72	0.408	0.557	1.577E-08	3.468E-08	100.8
		66.35	0.648	0.800	2.647E-08	1.406E-07	16.6
		82.3	0.809	0.962	2.767E-08	2.261E-07	12.4
5.111(2)	3^-	42.72	0.407	0.555	2.303E-07	5.067E-07	11.7
		66.35	0.646	0.798	1.334E-07	7.086E-07	5.1
		82.3	0.808	0.961	7.751E-08	6.336E-07	6.5
5.367(7)		42.72	0.406	0.553	1.024E-07	2.253E-07	20.3
5.484(23)	4^+	82.3	0.806	0.958	6.270E-09	5.125E-08	52.6
5.653(3)	3^-	42.72	0.404	0.551	9.013E-08	1.983E-07	24.4
		66.35	0.644	0.794	8.913E-08	4.733E-07	7.4
		82.3	0.805	0.957	5.678E-08	4.641E-07	8.6
5.765(11)	3^-	66.35	0.643	0.794	1.699E-08	9.021E-08	28.0
5.811(21)	2^+	42.72	0.403	0.550	2.686E-08	5.914E-05	59.1
5.929(8)	3^-	42.72	0.403	0.550	2.641E-08	5.812E-08	64.8
		66.35	0.637	0.786	8.588E-08	4.561E-07	8.0
		82.3	0.804	0.956	7.536E-08	6.160E-07	7.3
6.076(5)		42.72	0.402	0.548	5.392E-08	1.187E-07	34.0
		66.35	0.642	0.792	2.428E-08	1.290E-07	22.6
		82.3	0.803	0.955	2.231E-08	1.823E-07	18.1
6.308(3)	(2^+)	42.72	0.401	0.547	1.028E-07	2.263E-07	25.1
		66.35	0.640	0.791	1.038E-07	5.462E-07	6.3
		82.3	0.802	0.954	6.651E-08	5.440E-07	6.4
6.422(2)	(2^+)	42.72	0.400	0.546	1.209E-07	2.662E-07	23.4
		66.35	0.640	0.790	1.232E-07	6.619E-07	7.6
		82.3	0.801	0.953	7.619E-08	6.321E-07	10.2

5. Model Comparison and Discussion

5.1 Calculations for ^{32}S

For an unambiguous multipolarity assignment and an almost model independent determination of the transition strength at the photon point, a PWBA analysis (see chapter 2.2) can be applied for electron scattering data of a nucleus with low Z and at low momentum transfer q , as in the case of ^{32}S . In this work a PWBA calculation for the second 2^+ state ($E_x = 4.28$ MeV) in ^{32}S was performed. The experimental cross sections are multiplied by a DWBA correction factor in order to include the Coulomb distortion effects. These factors were extracted from a comparison of DWBA and PWBA cross section calculations for the given kinematics with the code PAMELA [46].

Terms up to the order $l=3$ were included in the expression [Eq. (2.31)]. The transition radii R_r^6 and R_r^4 were correlated [47] with R_r^2 through the relations $R_r^4 = 1.09(R_r^2)^2$ and $R_r^6 = 1.18(R_r^2)^3$. These coefficients were obtained from the radial moments calculated with the code PAMELA.

In Fig 4.6 the results for $\lambda = 1, 2, 3$ assuming an electric transition are shown. The multipolarity assignment is based on the best χ^2 and the condition of a value for the transition radius reasonably close to the root-mean-square charge radius of ^{32}S ($R_c = 3.23$ fm) [44]. The best agreement with the data is achieved assuming $\lambda = 2$. Here for $\lambda = 1$ the transition radius R_r is not defined at all. At $\lambda = 3$ the χ^2 is smaller than at $\lambda = 2$, but the transition radius R_r deviates from the root-mean-square charge radius R_c very strongly. The transition strength $B(C2) = (51 \pm 15) \text{ e}^2\text{fm}^4$ extracted

from this analysis is in a good agreement with an NRF experiment [48] which provides $B(C2) = (46.4 \pm 7.7) e^2 \text{fm}^4$.

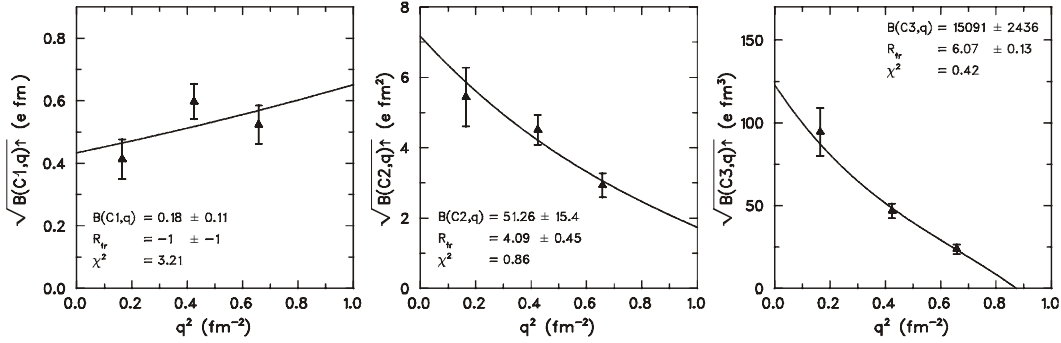


Fig. 4.6: The PWBA analysis for the excitation of the 2^+ state at $E_x = 4.28$ MeV assuming an E1 (left), an E2 (middle), or an E3 (right) transition.

The form factors and cross sections data deduced from the present experiment provide a good test of the microscopic calculations. Shell model wave functions were obtained from the unified *sd*-shell (USD) interaction [49], which has been shown to provide an excellent description of static and dynamic properties in *sd*-shell nuclei [27]. For the description of the E2 transition strengths effective *g* factors were employed. The effective *g* factors are available from the empirical fit of Brown and Wildenthal (BW) for *sd*-shell nuclei [50].

The experimental cross sections for the second 2^+ state in ^{32}S together with the shell model predictions are shown in Fig. 4.7. The dashed, dotted and solid lines represent longitudinal, transverse and total cross sections, respectively. These calculations predict a clear dominance of transverse over longitudinal cross sections for the experimental kinematics.

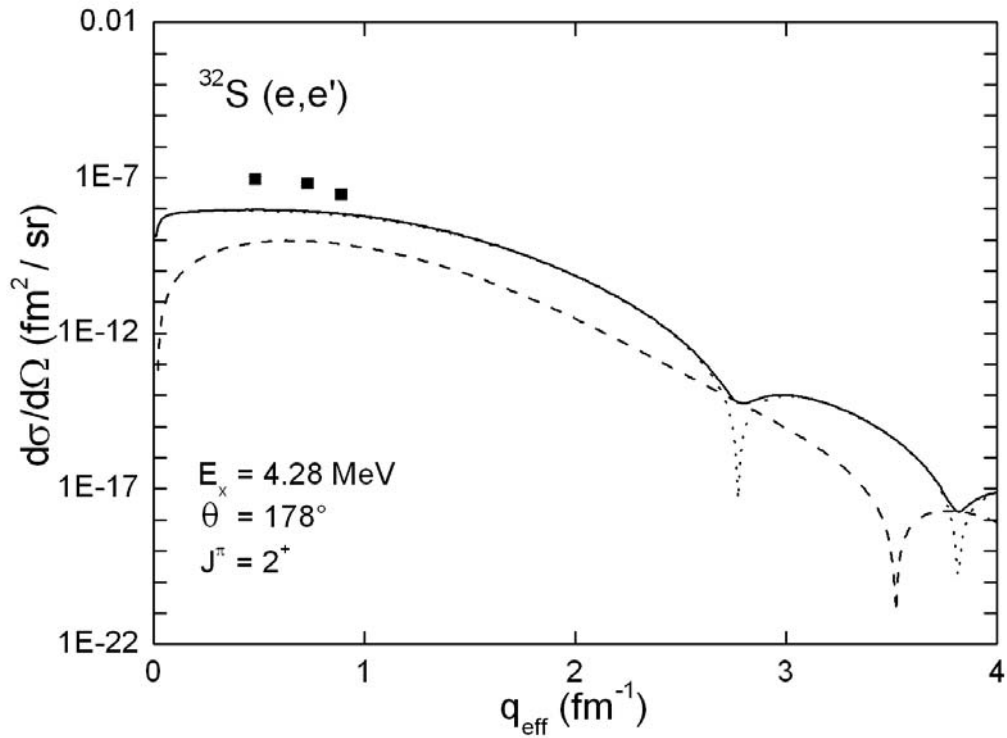


Fig. 4.7: Cross sections for the E2 transition to the $J^\pi = 2^+$ state at $E_x = 4.28$ MeV in ^{32}S . The squares present the experimental data. The error bars are smaller than the size of the data points. The dashed, dotted and solid lines represent the longitudinal, transverse and total cross sections, respectively, predicted by the shell model calculation.

In order to extract the transition strength the total cross section needs to be scaled to the experimental points. In Fig. 4.8 the total cross section normalized by a factor 6.5 is shown. The transition strength $B(C2) = 49.14 \text{ e}^2\text{fm}^4$ extracted from this approach is in good agreement with the PWBA analysis and the result of the NRF experiment.

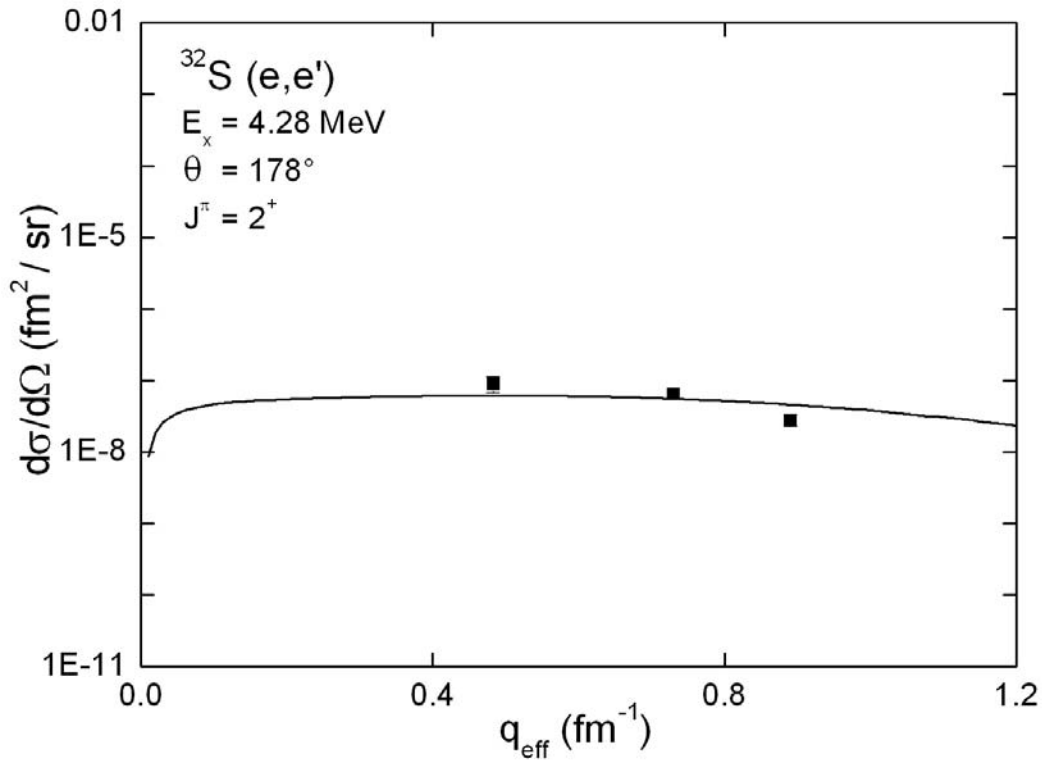


Fig. 4.8: Total cross section for the E2 transition ($E_x = 4.28$ MeV) in ^{32}S predicted by the shell model calculation. The solid curve is normalized to describe the data (squares).

5.2 Comparison with Quasiparticle-Phonon Model Calculations.

Experimental $^{58}\text{Ni}(e,e')$ and $^{90}\text{Zr}(e,e')$ cross sections are compared with the prediction of the microscopic Quasiparticle-Phonon Model (QPM). The basics of the model are described in chapter 2.6. The calculations have been performed with wave functions for excited states which include one-, two- and three-phonon configurations [see Eq. (2.42)]. At present, the calculations were restricted to 2^+ and 3^- states in ^{58}Ni and ^{90}Zr , respectively. The one-, two- and three-phonon configurations are built from phonons with spin-parity ranging from 1^\pm to 6^\pm and with excitation energies up to 15 MeV, 9 MeV, and 10 MeV, respectively.

After calculating the transition current and magnetization densities of each state the DWBA (e,e') cross sections for the excitation of these states were obtained [51].

5.2.1 Calculations for ^{58}Ni

For ^{58}Ni the transverse form factors are available only at two momentum transfers, and therefore, the discussion is restricted to transitions populating $J^\pi = 2^+$ states. Figure 4.9 presents the example of longitudinal (bottom), transverse (middle), and total (top) cross sections predicted by the QPM at 65 MeV incident energy for E2 transitions in ^{58}Ni . The results show that at 180° the transverse part of the cross section always dominates over the longitudinal, the contribution of which is typically restricted to at most a few percent. Even for the most collective transition for to 2_1^+ state, the longitudinal cross section amounts to 3.8% only. The calculations also show that the most prominent transverse transitions do not have the largest $B(E2)$ values at the photon point.

The figures 4.10 and 4.11 compare the theoretical predictions of cross sections for E2 transitions with the experimental results from the present work for ^{58}Ni , for the range of excitation energy covered by the experiment. The experimental cross sections are shown in the upper part and the QPM predictions in the lower part of each plot.

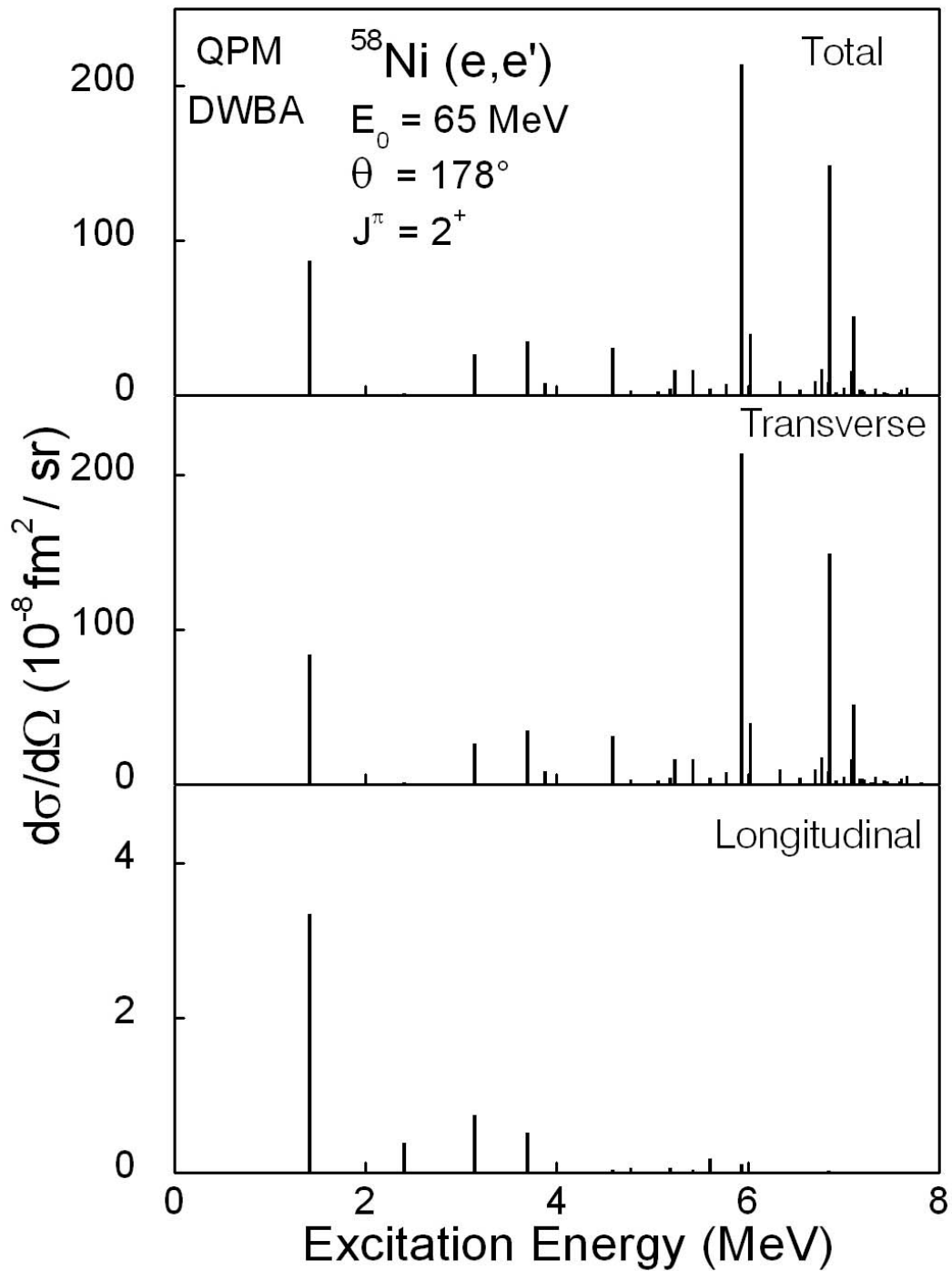


Fig. 4.9: Longitudinal, transverse, and total cross sections predicted by the QPM for the excitation of E2 transitions in ^{58}Ni for inelastic electron scattering at 180° . The incident energy is 65 MeV. Note the different y-scales of the transverse and longitudinal parts.

The location of large E2 transitions is predicted well by the QPM calculations for ^{58}Ni in the excitation energy region up to 5 MeV. Two fragmentation regions are predicted for ^{58}Ni at the excitation energies about 3.5 and 6 MeV, which are in agreement with the experimental results. While the qualitative reproduction is quite good, a quantitative overestimation, i.e. a quenching, by almost an order of magnitude is observed.

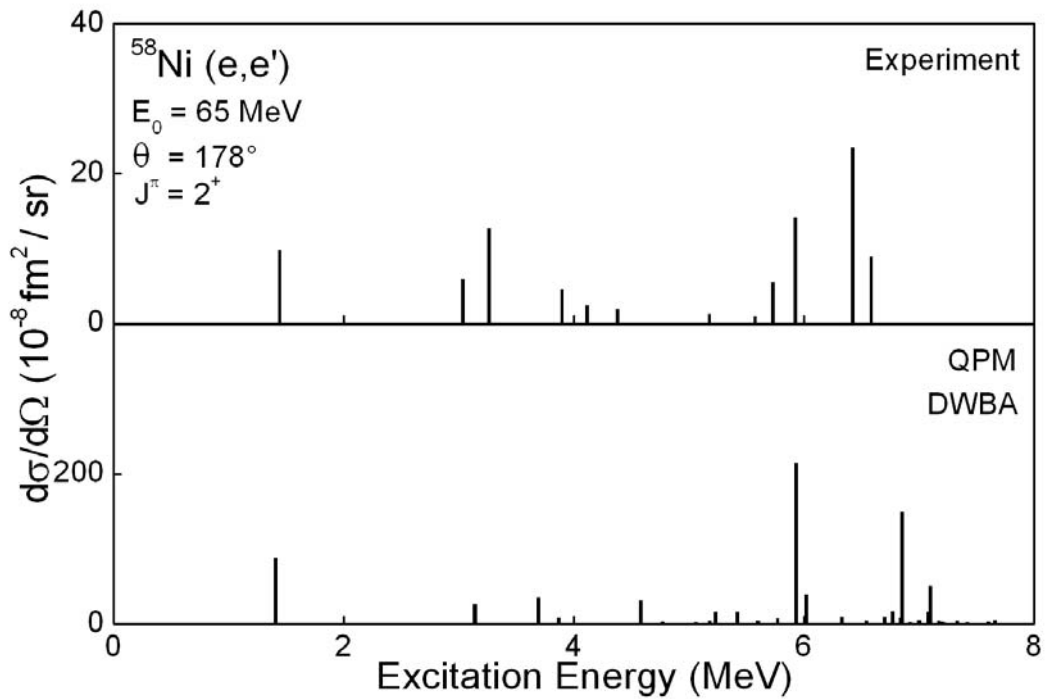


Fig. 4.10: Comparison of the cross sections for E2 transitions in ^{58}Ni from the present work (top) with QPM calculations (bottom). The incident energy is 65 MeV. The effective scattering angle is 178 degree. Note the different y-scales for the experimental and theoretical cross sections.

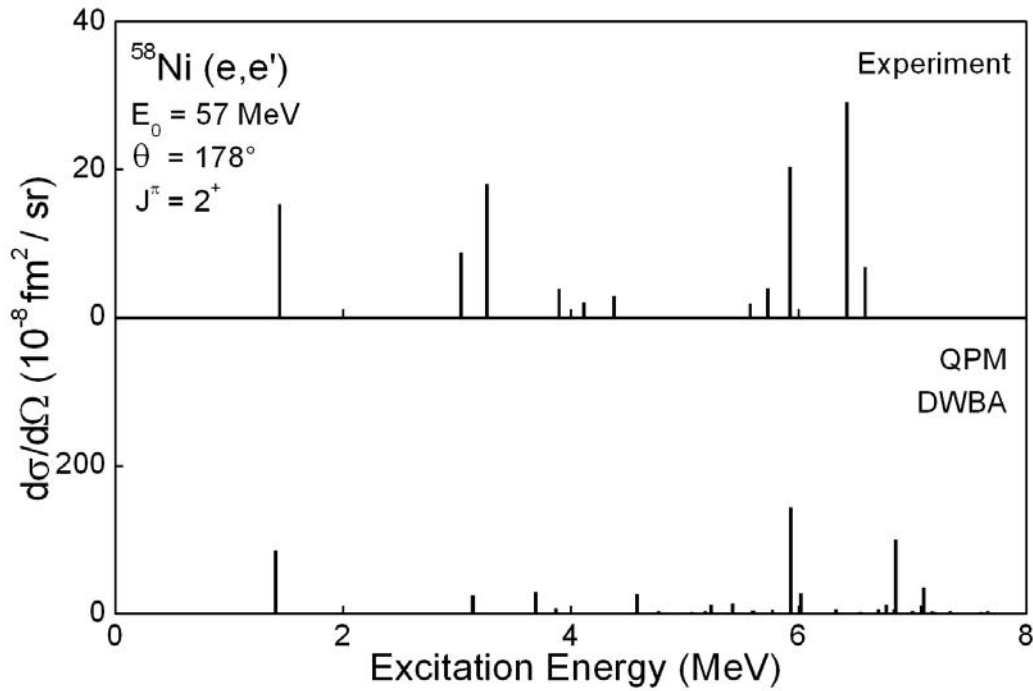


Fig. 4.11: Comparison of the cross sections for E2 transitions in ^{58}Ni from the present work (top) with QPM calculations (bottom). The incident energy is 57 MeV. The effective scattering angle is 178 degree. Note the different y-scales between experimental and theoretical cross sections.

Figure 4.12 shows the comparison of transverse and longitudinal cross sections for the two most prominent transitions predicted by the QPM in ^{58}Ni as a function of the incident electron energy E_0 . The effective scattering angle θ_{eff} is 178° . It becomes apparent that the transverse part always dominates over longitudinal and peaks at much higher incident energy for each transition. The energy dependence is also different between the collective (2_1^+ , $E_x = 1.41 \text{ MeV}$) and two-quasiparticle (2_{16}^+ , $E_x = 5.93 \text{ MeV}$) transitions, which have different structure. The first one is formed due to collective surface excitations of a nucleus (charge excitations), whereas the second one is a combination of current excitations.

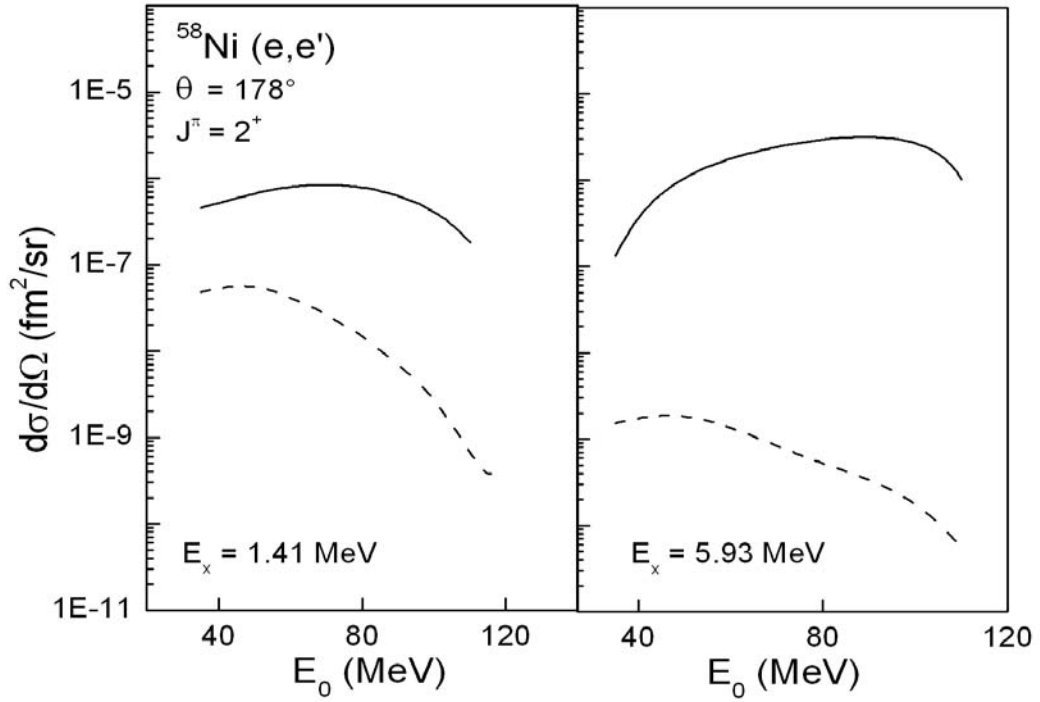


Fig.4.12: Comparison of the QPM predictions for the (e,e') transverse (solid line) and longitudinal (dashed line) cross sections of the two most prominent E2 transitions in ^{58}Ni as function of incident electron energy E_0 .

A comparison of the cross sections for the two most prominent E2 transitions in ^{58}Ni as function of the scattering angle θ is shown in the Fig. 4.13. For the collective low-lying transition at $E_x = 1.41$ MeV the longitudinal cross section is always dominating over the transverse cross section except for backward angles $\theta \geq 170^\circ$. Thus transverse form factors of collective electric modes in the low-energy spectra can be studied only at angles very close to $\theta = 180^\circ$. For the two-quasiparticle transition at $E_x = 5.93$ MeV the transverse part dominates over the longitudinal one already at much smaller angles $\theta \geq 115^\circ$. Thus, the prominent transverse electric quasiparticle excitations can typically be studied at scattering angles in the region

from about 120 to 180 degrees. Such kind of measurements can also be carried out at the high resolution Lintott magnetic spectrometer.

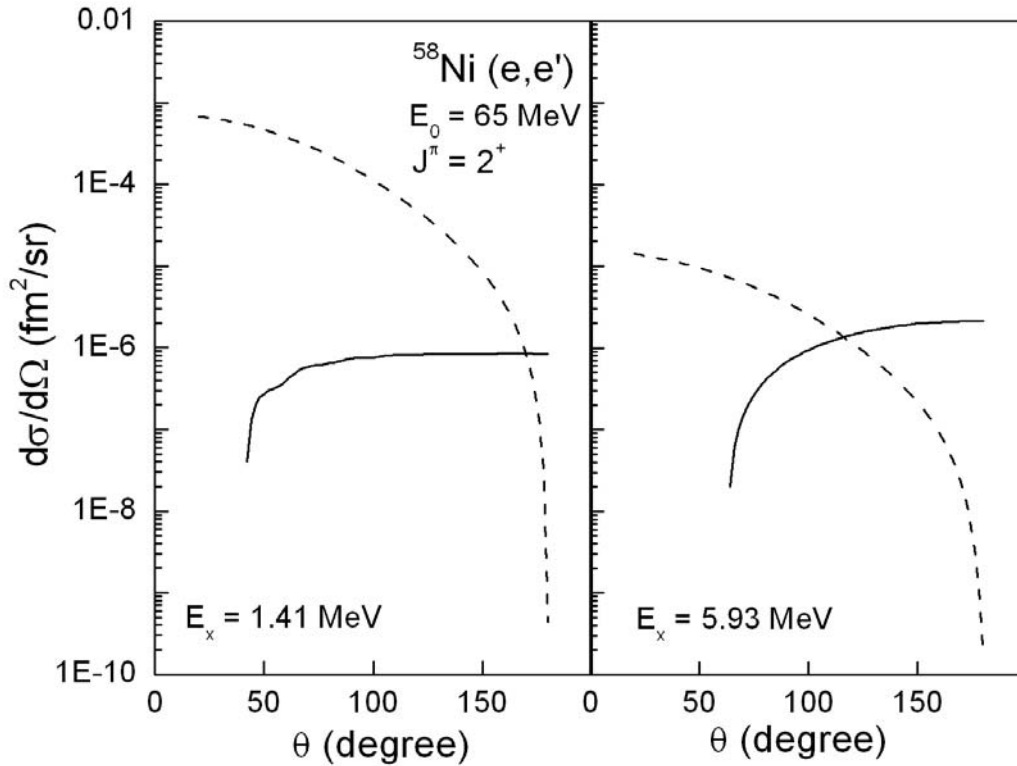


Fig. 4.13: Comparison of the QPM predictions for the (e,e') transverse (solid line) and longitudinal (dashed line) cross sections of the two most prominent E2 transitions in ⁵⁸Ni as function of scattering angle θ .

5.2.2 Calculations for ⁹⁰Zr

In this section the cross sections for the population of 3⁻ states in ⁹⁰Zr are discussed. Experimental data are available at three incident energies, which correspond to the momentum transfers from 0.37 fm⁻¹ to 0.82 fm⁻¹. The figures 4.14 – 4.16 compare the experimental results with the QPM predictions of cross sections for E3 transitions in ⁹⁰Zr measured only for E_x > 3 MeV, i.e. the 3₁⁻ state at E_x = 2.748 MeV is not observed. The experimental cross sections are shown in the upper part and the QPM cross sections in the lower part of each plot.

Because of the experimental thresholds only a reduced number of experimental states can be observed with respect to the QPM calculations. Like for E2 transitions in ^{58}Ni , for E3 transitions in ^{90}Zr the transverse part of the cross section always dominates over the longitudinal one. An exclusion is the most collective transition to the 3_1^- state at excitation energy $E_x = 3.14$ MeV, where the longitudinal contribution amounts to 69, 8.6, and 2% at incident energies 42.7, 66.4, and 82.3 MeV, respectively.

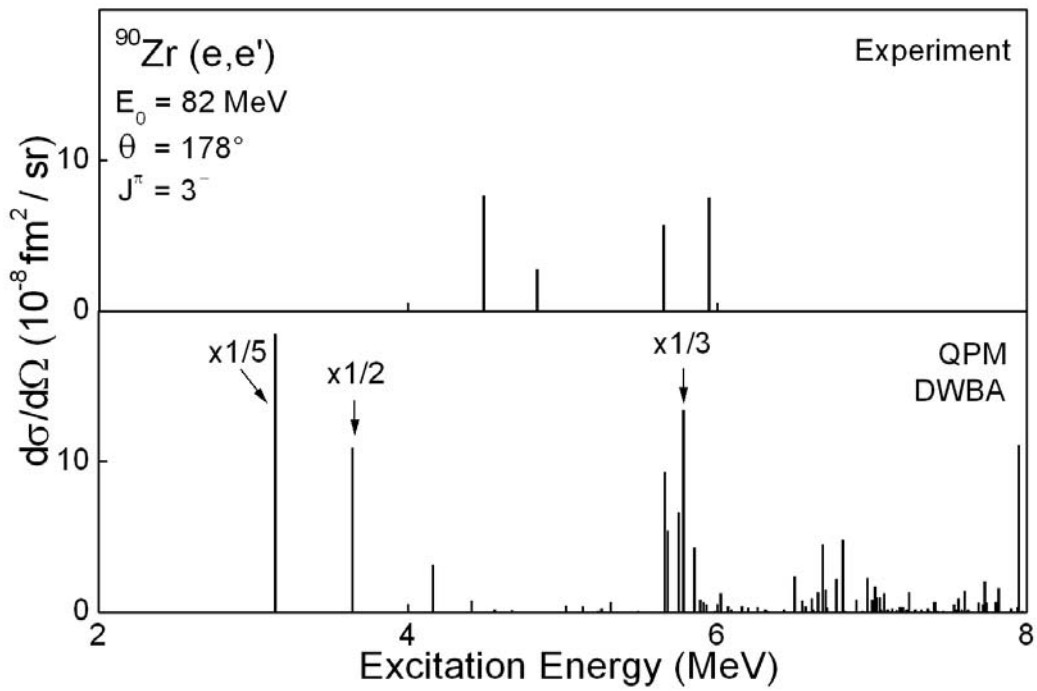


Fig. 4.14: Comparison of the cross sections for E3 transitions in ^{90}Zr from the present work (top) with QPM calculations (bottom). The incident energy is 82 MeV. The effective scattering angle is 178 degree.

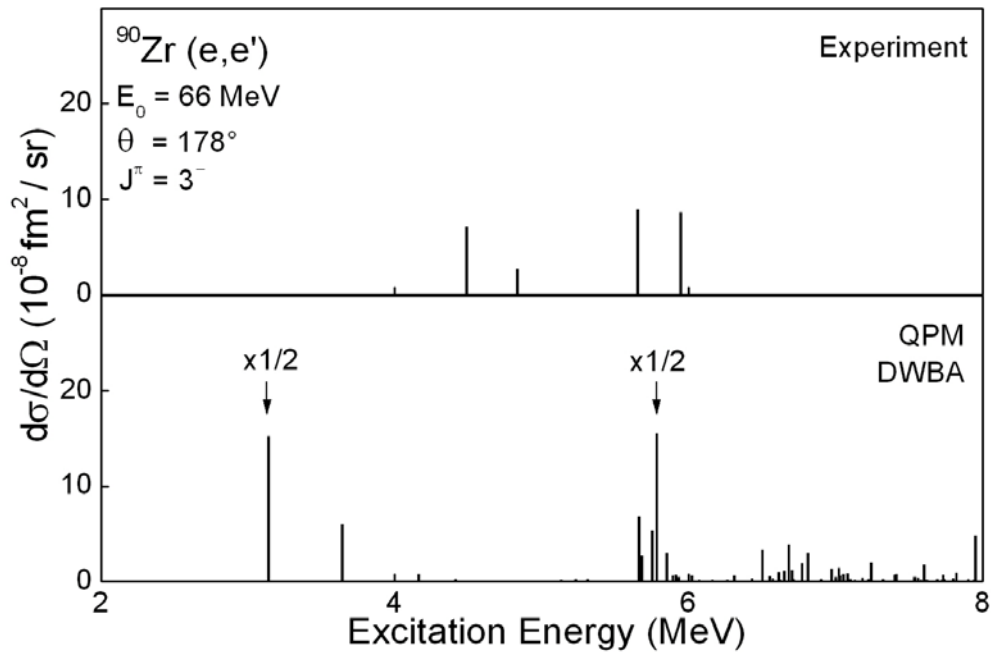


Fig. 4.15: Comparison of the cross sections for E3 transitions in ^{90}Zr from the present work (top) with QPM calculations (bottom). The incident energy is 66 MeV. The effective scattering angle is 178 degree.

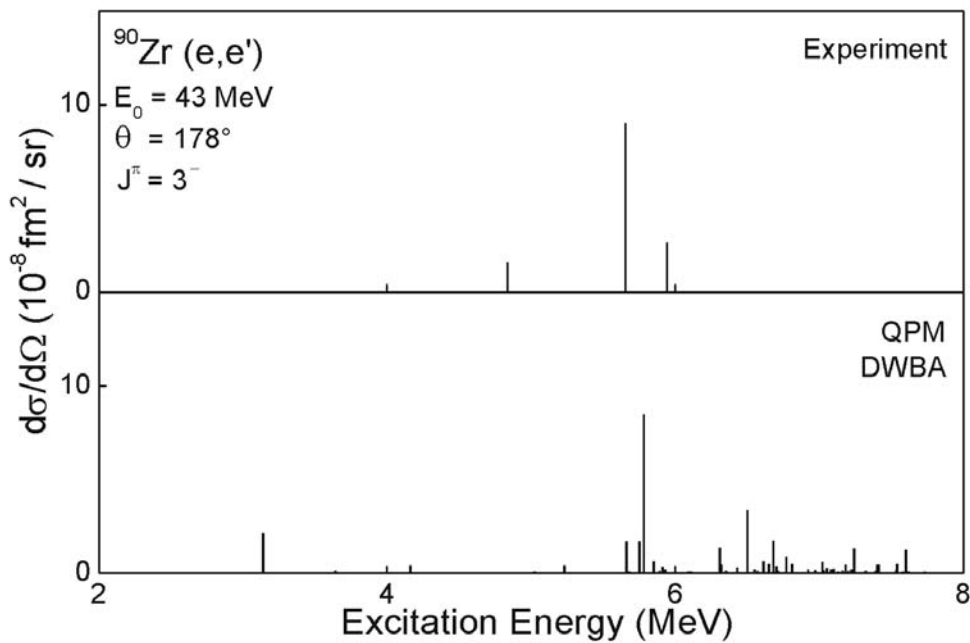


Fig. 4.16: Comparison of the cross sections for E3 transitions in ^{90}Zr from the present work (top) with QPM calculations (bottom). The incident energy is 43 MeV. The effective scattering angle is 178 degree.

The strengths around 6 MeV predicted by the QPM seems to be confirmed by the data. The first E3 transition at excitation energy $E_x = 2.748$ MeV is not observed in the experiment, because the spectra were measured only at excitation energies above 3 MeV. The two lowest transitions observed in the experiment lie at higher energies compared to the QPM predictions. They are shifted about by 1 MeV. On the average the QPM calculations overpredict the experimental cross sections by a factor of 2 – 3.

6. Summary and Outlook

Electron scattering at 180° provides numerous advantages for the study of nuclear structure: precise knowledge of the reaction mechanism, the ability to vary independently the momentum and energy transferred to the nucleus. Scattering experiments provide detailed information on nuclear radii, ground state, and transition charge densities, as well as the spatial distribution of intrinsic magnetic and convection currents.

An analysis of the available 180° data measured at the S - DALINAC provides evidence for electric excitations in all studied nuclei at low excitation energy. Comparison to microscopic approaches, such as the shell model and the Quasiparticle-Phonon Model, shows that the cross sections are almost purely *transverse*. Even for low-energy collective phonons the contribution of the longitudinal part usually amounts to a few percent only. The momentum transfer dependence of transverse cross sections differs significantly from longitudinal ones for each transition as well as for different transitions. This fact causes difficulties in identifying unknown spin-parity characteristics of observed states.

The comparison of the experimental data with microscopic approaches plays an important role in understanding the structure of nuclei. In the present work the model predictions of the form factors agree reasonably with the limited data presently available, but significant quenching is observed in all cases.

Based on the present findings, electron scattering at 180° is a promising tool to the future experimental projects including the measurement of transverse electric transition strengths:

1. a detailed mapping of collective low-lying states in spherical and deformed nuclei [52 – 54];
2. search for a transverse E1 resonance below the GDR, the so-called toroidal mode [55, 56].

References

- [1] H. Überall, *Electron Scattering from Complex Nuclei* (Academic Press, New York - London, 1971).
- [2] R. Hofstadter, *Electron scattering and Nuclear and Nucleon Structure*, (Benjamin, New York, 1963).
- [3] T. DeForest, Jr. and J.D. Walecka, *Adv. Phys.* **15** (1966) 2.
- [4] A. Richter, *Proceedings of the Fifth European Particle Accelerator Conference*, ed. S. Meyers et al., (IOP Publishing, Bristol, 1996) 110.
- [5] S. Döbert, R. Eichhorn, H. Genz, H.-D. Gräf, R. Hahn, T. Hampel, S. Kostial, H. Loos, M. Reichenbach, A. Richter, E. Spamer, A. Stascheck, M. Thomas, O. Titze, T. Wesp, *Proceedings of the XVIII International Linac Conference*, Eds. C. Hill, M. Vretenar, CERN 96-07, Geneva (1996) 260.
- [6] M. Knirsch, *Dissertation D17*, TH Darmstadt (1991).
- [7] H. Diesener, U. Helm, G. Herbert, V. Huck, P. von Neumann-Cosel, C. Rangacharyulu, A. Richter, G. Schrieder, A. Stascheck, A. Stiller, J. Ryckebusch, and J. Carter, *Phys. Rev. Lett.* **72** (1994) 1994.
- [8] C. Lüttge, C. Hofmann, J. Horn, F. Neumeyer, A. Richter, G. Schrieder, E. Spamer, A. Stiller, D.I. Sober, S.K. Matthews, and L.W. Fagg, *Nucl. Instr. and Meth.* **A366** (1995) 325.
- [9] C. Lüttge, P. von Neumann-Cosel, F. Neumeyer and A. Richter, *Nucl. Phys.* **A606** (1996) 183.

- [10] H. Diesener, U. Helm, P. von Neumann-Cosel, A. Richter, G. Schrieder, A. Stascheck, A. Stiller, J. Carter, Nucl. Phys. **A696** (2001) 272.
- [11] A. Hotta, R.S. Hicks, R.L. Huffman, and G.A. Peterson, Phys. Rev. **C36** (1987) 2212.
- [12] L.W. Fagg, Rev. Mod. Phys. **47** (1975) 683.
- [13] B. Reitz, F. Hofmann, P. von Neumann-Cosel, F. Neumeyer, C. Rangacharyulu, A. Richter, G. Schrieder, D. I. Sober, and B. A. Brown, Phys. Rev. Lett. **82** (1999) 291.
- [14] P. von Neumann-Cosel, F. Neumeyer, B. Reitz, A. Richter, and J. Wambach, Phys. Rev. **C62** (2000) 034307.
- [15] F. Hofmann, P. von Neumann-Cosel, F. Neumeyer, C. Rangacharyulu, B. Reitz, A. Richter, G. Schrieder, D.I. Sober, L.W. Fagg, and B.A. Brown, Phys. Rev. **C65** (2002) 023411.
- [16] P. von Neumann-Cosel, F. Neumeyer, S. Nishizaki, V.Yu. Ponomarev, C. Rangacharyulu, B. Reitz, A. Richter, G. Schrieder, D.I. Sober, T. Waindzoeh, and J. Wambach, Phys. Rev. Lett. **82** (1999) 1105.
- [17] B. Reitz, A.M. van den Berg, D. Frekers, F. Hofmann, M. de Huu, Y. Kalmykov, H. Lenske, P. von Neumann-Cosel, V.Yu. Ponomarev, S. Rakers, A. Richter, G. Schrieder, K. Schweda, J. Wambach, and H.J. Wörtche, Phys. Lett. **B532** (2002) 179.
- [18] J.D. Bjorken and S.D. Drell, Relativistic Quantum Mechanics, New York (1964).
- [19] J.D. Bjorken and S.D. Drell, Relativistic Quantum Fields, New York (1965).

- [20] F.H. Lewis, Jr. and J.D. Walecka, Phys. Rev. **133** (1964) B849.
- [21] H. Theissen, Springer Tracts of Modern Physics **65**, (Springer, Heidelberg, 1972) 1.
- [22] M. Rosen, R. Raphael, and H. Überall, Phys. Rev. **163** (1967) 927.
- [23] A.J.F. Siegert, Phys. Rev. **52** (1937) 787.
- [24] B.T. Chertok, W.T.K. Johnson, and D. Sarkar, *Table of Coulomb Distortion Corrections to Inelastic Electron Scattering Cross Sections for Magnetic Dipole and – Quadrupole Transitions*, The American University, Dept. of Physics, Washington D.C. (1970).
- [25] M.G. Mayer and J.H.D. Jensen, *Elementary Theory of Nuclear Structure*, (Wiley, New York, 1955).
- [26] J.B. McGrory and B.H. Wildenthal, Ann. Rev. Nucl. Part. Sci. **30** (1980) 383.
- [27] B.A. Brown and B.H. Wildenthal, Ann. Rev. Nucl. Part. Sci. **38** (1988) 29.
- [28] V.G. Soloviev, *Theory of Complex Nuclei*, (publisher, Oxford, 1976).
- [29] A.I. Vdovin and V.G. Soloviev, Yad. Fiz. **14** (1983) 237.
- [30] R.K.J. Sandor, H.P. Blok, U. Garg, M.N. Harakeh, C.W. de Jager, V.Yu. Ponomarev, A.I. Vdovin, and H. de Vries, Phys. Lett. **B233** (1989) 54.
- [31] V.G. Soloviev, Ch. Stoyanov, and R. Nikolaeva, Izv. Akad. Nauk SSSR Ser. Fiz. **47** (1983) 2082.
- [32] A. Richter, Phys. Bl. **54** (1998) 31.

- [33] M. Brunken, S. Döbert, R. Eichhorn, H. Genz, H.-D. Gräf, H. Loos, A. Richter, B. Schweizer, A. Stascheck, and T. Wesp, Nucl. Instrum. Methods **A429** (1999) 21.
- [34] C. Lüttge, C. Hofmann, J. Horn, F. Neumeyer, A. Richter, G. Schrieder, E. Spamer, A. Stiller, D.I. Sober, S.K. Matthews, and L.W. Fagg, Nucl. Instrum. Methods **A366** (1995) 325.
- [35] M. Knirsch, Dissertation D17, TH Darmstadt (1991).
- [36] H. Diesener, U. Helm, G. Herbert, V. Huch, P. von Neumann-Cosel, C. Rangacharyulu, A. Richter, G. Schrieder, A. Stascheck, A. Stiller, J. Ryckebusch, and J. Carter, Phys. Rev. Lett. **72** (1994) 1994.
- [37] K.D. Hummel, Dissertation D17, TH Darmstadt (1992).
- [38] F. Neumeyer, Dissertation D17, TH Darmstadt (1997).
- [39] B. Reitz, Diploma thesis, TH Darmstadt (1996).
- [40] B. Reitz, Dissertation D17, TH Darmstadt (2000).
- [41] S. Strauch, Diploma thesis, TH Darmstadt (1993).
- [42] F. Neumeyer, Diploma thesis, TH Darmstadt (1993).
- [43] L.I. Schiff, Phys. Rev. **87** (1952) 750.
- [44] G. Fricke, C. Bernhardt, K. Heilig, L.A. Schaller, L. Schellenberg, E.B. Shera, and C.W. de Jager, At. Data Nucl. Data Tables **60** (1995) 177.
- [45] R.G. Helmer, M.A. Lee, Nucl. Data Sheets **61** (1990) 93; Evaluated Experimental Nuclear Structure Data File, National Nuclear Data Center Brookhaven, NY, 2003; <http://www.nndc.bnl.gov/>
- [46] F. Hofmann (private communication).

- [47] N. Petraitis, J.P. Connelly, H. Crannell, L.W. Fagg, J.T. O'Brien, D.I. Sober, J.R. Deininger, S.E. Williamson, R.A. Lindgren, and S. Raman, *Phys. Rev.* **C49** (1994) 3000.
- [48] U.E.P. Berg, K. Ackermann, K. Bangert, C. Bläsing, W. Naatz, R. Stock, K. Weinhard, M.K. Brussel, T.E. Chapuran, and B.H. Wildenthal, *Phys. Lett.* **140B** (1981) 191.
- [49] B.H. Wildenthal, *Prog. Part. Nucl. Phys.* **11** (1984) 5.
- [50] B.A. Brown and B.H. Wildenthal, *Nucl. Phys.* **A474** (1987) 290.
- [51] V.Yu. Ponomarev (private communication).
- [52] E. Moya de Guerra and A.E.L. Dieperink, *Phys. Rev.* **C18** (1978) 1596.
- [53] E. Moya de Guerra and S. Kowalski, *Phys. Rev.* **C22** (1980) 1308; **C20** (1979) 357.
- [54] E. Moya de Guerra, *Ann. Phys. (N.Y.)* **128** (1980) 286.
- [55] N. Ryezayeva, T. Hartmann, Y. Kalmykov, H. Lenske, P. von Neumann-Cosel, V. Yu. Ponomarev, A. Richter, A. Shevchenko, S. Volz, and J. Wambach, *Phys. Rev. Lett.* **89** (2002) 272502.
- [56] D. Vretenar, N. Paar, P. Ring, and T. Nikšić, *Phys. Rev.* **C65** (2002) 021301.

Acknowledgement

I would like to thank all persons who have helped me during this work.

On the first place I would like to sincerely thank *Professor Dr. Dr. h.c. mult. Achim Richter* for giving me the great opportunity to work on such an exciting topic under his supervision.

Also I would like to thank *Privatdozent Dr. Peter von Neumann-Cosel* for useful discussions during the realization of this diploma thesis and for reading the thesis.

I address my heartfelt gratitude to *Dr. Harald Genz* for his every day help, care and support.

I am very grateful to *Dr. Frank Hofmann* for introducing me to the topic, various discussions and for his qualified and friendly patronage.

I thank *Dr. V. Yu. Ponomarev* for his great support concerning the QPM calculations and for various valuable discussions.

I would like to express my gratitude also to *Dr. Sergiy Khodyachykh, Oleksiy Burda, Yaroslav Kalmykov, Artem Shevchenko, Natalya Ryezayeva, Olena Yevetska, and Inna Pysmenetska* for numerous significant advices.

I am grateful to *Dr. Shmatko, Dr. Afanasiev, Dr. Shchus* and Chair of the Experimental Nuclear Physics of the Karazin Kharkiv National University (Ukraine) for the time they have spent for my education.

Finally, my heartfelt gratitude to my family – my stepfather *Vasiliy*, my mother *Valentyna*, and my brother *Oleksiy*. Your thoughts

and your care were supporting me very much during my study in the Karazin Kharkiv National University and during my stay in Darmstadt.